Mechanisms of Low-Frequency Variability in North Atlantic Ocean Heat Transport and AMOC

DYLAN OLDENBURG,[a] ROBERT C. J. WILLS,[b] KYLE C. ARMOUR,[a,b] LUANNE THOMPSON,[a] AND
LAURA C. JACKSON[c]

[a] School of Oceanography, University of Washington, Seattle, Washington
[b] Department of Atmospheric Sciences, University of Washington, Seattle, Washington
[c] Met Office Hadley Centre, Exeter, United Kingdom

ABSTRACT: Ocean heat transport (OHT) plays a key role in climate and its variability. Here, we identify modes of low-frequency North Atlantic OHT variability by applying a low-frequency component analysis (LFCA) to output from three global climate models. The first low-frequency component (LFC), computed using this method, is an index of OHT variability that maximizes the ratio of low-frequency variance (occurring at decadal and longer time scales) to total variance. Lead–lag regressions of atmospheric and ocean variables onto the LFC time series illuminate the dominant mechanisms controlling low-frequency OHT variability. Anomalous northwesterly winds from eastern North America over the North Atlantic act to increase upper ocean density in the Labrador Sea region, enhancing deep convection, which later increases OHT via changes in the strength of the Atlantic meridional overturning circulation (AMOC). The strengthened AMOC carries warm, salty water into the subpolar gyre, reducing deep convection and weakening AMOC and OHT. This mechanism, where changes in AMOC and OHT are driven primarily by changes in Labrador Sea deep convection, holds not only in models where the climatological (i.e., time-mean) deep convection is concentrated in the Labrador Sea, but also in models where the climatological deep convection is concentrated in the Greenland–Iceland–Norwegian (GIN) Seas or the Irminger and Iceland Basins. These results suggest that despite recent observational evidence suggesting that the Labrador Sea plays a minor role in driving the climatological AMOC, the Labrador Sea may still play an important role in driving low-frequency variability in AMOC and OHT.

KEYWORDS: Meridional overturning circulation; Climate variability; Atmosphere-ocean interaction; Statistical techniques; Energy transport; Coupled models; Oceanic variability

1. Introduction

The oceans play a major role in global climate by transporting heat from low to high latitudes (e.g., Ganachaud and Wunsch 2000). The Atlantic Ocean is of particular relevance to global climate because its meridional ocean heat transport (OHT) is northward in both hemispheres, unlike in the Pacific (e.g., Peixoto and Oort 1993), owing to the existence of a strong Atlantic meridional overturning circulation (AMOC) (Ganachaud and Wunsch 2003). Both AMOC and Atlantic OHT experience robust variability at decadal and longer time scales in global climate models (e.g., Delworth and Zeng 2016). This variability in Atlantic OHT leads to major changes in North Atlantic climate (e.g., Covey and Thompson 1989). Variations in mid-latitude North Atlantic OHT are also linked to changes in OHT into the Nordic seas that can impact Arctic sea ice cover (e.g., Day et al. 2012; Zhang 2015; Oldenburg et al. 2018).

To understand low-frequency Atlantic OHT variability, it is important to study the driving mechanisms. Mechanisms of this variability have been widely analyzed using low-pass filtered model output (Dong and Sutton 2001, 2002, 2003, 2005), where low-frequency variability is defined as variability at decadal and longer time scales. These analyses suggest that AMOC variability controls low-frequency OHT variability. Analyses of different low-frequency AMOC indices, such as the first principal component (PC) of the low-pass filtered MOC or a

convective index, all show that density anomalies in high-latitude deep-convection regions precede changes in AMOC on these time scales (Delworth et al. 1993; Danabasoglu et al. 2012b; Tulloch and Marshall 2012).

Low-frequency variations in AMOC and OHT are closely linked to changes in North Atlantic sea surface temperatures (SSTs) and sea level pressure (SLP) (Bjerknes 1964; Kushnir 1994), both of which have exhibited substantial decadal and multidecadal variability in the twentieth century (e.g., Bjerknes 1964; Kushnir 1994; Schlesinger and Ramankutty 1994; Knight et al. 2005; Delworth et al. 2007; Ting et al. 2009; Deser et al. 2010). The North Atlantic Oscillation (NAO) appears to play a key role in driving these AMOC and SST fluctuations via surface buoyancy flux and wind stress changes (Eden and Jung 2001; Mecking et al. 2015; Delworth et al. 2016; Delworth and Zeng 2016; Kim et al. 2018, 2020). Delworth and Zeng (2016) use a series of model experiments to show that NAO-related anomalous heat fluxes in the subpolar gyre can drive cooling that results in increased upper ocean density in that region, increasing mixed layer depths and deep convection, resulting in a strengthening of AMOC and the associated OHT.

AMOC and its associated OHT are also closely related to the amount of water mass transformation (WMT) in the high-latitude regions of the North Atlantic (Marsh 2000; Isachsen et al. 2007; Grist et al. 2009; Josey et al. 2009; Langehaug et al. 2012b). The WMT is the conversion of a parcel from one density class to another via air–sea exchanges or mixing, and is typically described as a density flux. Surface-forced WMT can

be estimated from air–sea heat and freshwater fluxes (Walin 1982; Tziperman 1986; Speer and Tziperman 1992). This WMT allows subsequent deepwater formation, as evidenced by the deep mixed layers in many regions of the North Atlantic. In the North Atlantic, WMT occurs when the North Atlantic Current carries subtropical water northward, where it is cooled by air–sea fluxes, thereby becoming more dense and transforming into Subpolar Mode Water, which is the dominant water mass in the eastern subpolar region above the permanent pycnocline (Pérez-Brunius et al. 2004; McCartney and Talley 1982; Brambilla and Talley 2008).

Although there is a well-established link between AMOC and high-latitude WMT, there is debate about which high-latitude deep-water formation regions control AMOC and its variability. Recent observational analyses suggest that the Greenland–Iceland–Norwegian (GIN) Seas play a primary role, rather than the Labrador Sea (Chafik and Rossby 2019; Lozier et al. 2019; Petit et al. 2020; Zou et al. 2020). Global climate models (GCMs) differ in their representations of which North Atlantic deep convection regions control AMOC, and biases in the deep convection regions are coincident with biases in temperature and salinity relative to observations (Langehaug et al. 2012b; Menary et al. 2015b; Heuzé 2017). Several models from phase 5 of the Coupled Model Intercomparison Project (CMIP5, Taylor et al. 2012), such as NCAR's Community Climate System Model version 4 (CCSM4; Gent et al. 2011), show convection primarily occurring in the Labrador Sea (Danabasoglu et al. 2012b; Brodeau and Koenigk 2016). However, others, such as the Geophysical Fluid Dynamics Laboratory Earth System Model version 2M (GFDL-ESM2M; Dunne et al. 2012, 2013) and the Hadley Centre Global Environment Model version 3.1 (HadGEM3-GC3.1-LL; Kuhlbrodt et al. 2018; Roberts et al. 2019), show deep convection occurring in the GIN Seas, the Irminger and Iceland Basins, and the Labrador Sea. Although there has been much attention paid to which deep convection regions control climatological AMOC, a key question is whether the same regions also control low-frequency variability in AMOC and OHT.

There are two potential limitations of previous analyses of the causes of low-frequency variability in OHT. First, AMOC does not account for all of the low-frequency variability in Atlantic OHT, as it misses contributions from gyre circulation changes in response to surface wind and buoyancy flux anomalies (e.g., Eden and Jung 2001; Drijfhout and Hazeleger 2006; Menary et al. 2015a; Wills et al. 2019a). Thus, methods that composite OHT on AMOC or convective indices may be missing key contributions to low-frequency OHT variability. Second, using a PC analysis of low-pass filtered data results in a loss of temporal resolution, making it difficult to discern lead–lag relationships between variables on time scales less than the filtering period (Cane et al. 2017; Wills et al. 2019a). Here, we instead use a low-frequency component analysis (LFCA) applied directly to OHT. This method separates low-frequency from high-frequency variability based on differences in their latitudinal structure, while still retaining information about the high-frequency variability. LFCA is described in Wills et al. (2018) and has been applied to characterize and understand modes of low-frequency Atlantic and Pacific SST variability

(Wills et al. 2019a,b; Årthun et al. 2021). LFCA makes no a priori assumptions about which processes drive or contribute to OHT variability. Moreover, because the resulting indices of low-frequency variability are not low-pass filtered, it is possible to discern how high-frequency variations (e.g., in SLP and surface buoyancy fluxes) contribute to OHT variations at longer time scales. It is important to note that this method does not determine the sensitivity of the OHT and AMOC to changes in, for example, WMT in different deepwater formation regions. Instead, this method allows us to determine where WMT occurs preceding periods of enhanced OHT and AMOC. In other words, it combines an analysis of where the variance in WMT is concentrated with an analysis of where the ocean is sensitive to this variance.

Here, we use LFCA to determine which mechanisms are responsible for the decadal to multidecadal variability of Atlantic OHT. Specifically, we examine the role of AMOC and whether the mechanisms differ between models with different primary locations of climatological (i.e., time-mean) deep convection. We compare three fully coupled GCMs that span a range of climatological regions of deep convection: CCSM4, in which deep convection is primarily concentrated in the Labrador Sea; GFDL-ESM2M, in which deep convection is primarily concentrated in the Irminger and Iceland Basins; and HadGEM3-GC3.1-LL, in which the deep convection is primarily concentrated in the GIN Seas. Our low-frequency component analysis provides a novel view of the mechanisms of low-frequency AMOC variability, its role in OHT, and its links to WMT variability.

This paper is organized as follows. In section 2a, we describe the models used in this analysis. In section 2b, we compare and contrast the model climatologies of Atlantic OHT and ocean circulation. In section 2c, we describe the models' climatologies of AMOC in density space. In section 2d, we examine the surface-forced overturning streamfunction and water mass transformation in each model. In section 3, we compare the water mass transformation computed from model data to the water mass transformation calculated from observational datasets. In section 4, we use low-frequency component analysis and subsequent lead–lag regression analyses to elucidate the mechanisms of low-frequency OHT variability in the three models. In section 5, we summarize our results, describe our main conclusions, and make comparisons with the results from other studies.

2. Model climatologies

a. Description of models

We examine the mechanisms of low-frequency Atlantic OHT variability within three coupled atmosphere–ocean GCM simulations: a 1300-yr preindustrial control simulation of CCSM4 (Gent et al. 2011), a 500-yr preindustrial control simulation of GFDL-ESM2M (Dunne et al. 2012, 2013), and a 500-yr preindustrial control simulation of HadGEM3-GC3.1-LL (Kuhlbrodt et al. 2018; Roberts et al. 2019), all of which have ocean-model resolution of ~1° in the midlatitudes. All three simulations are forced with constant 1850s greenhouse

Winter mixed layer depth climatology

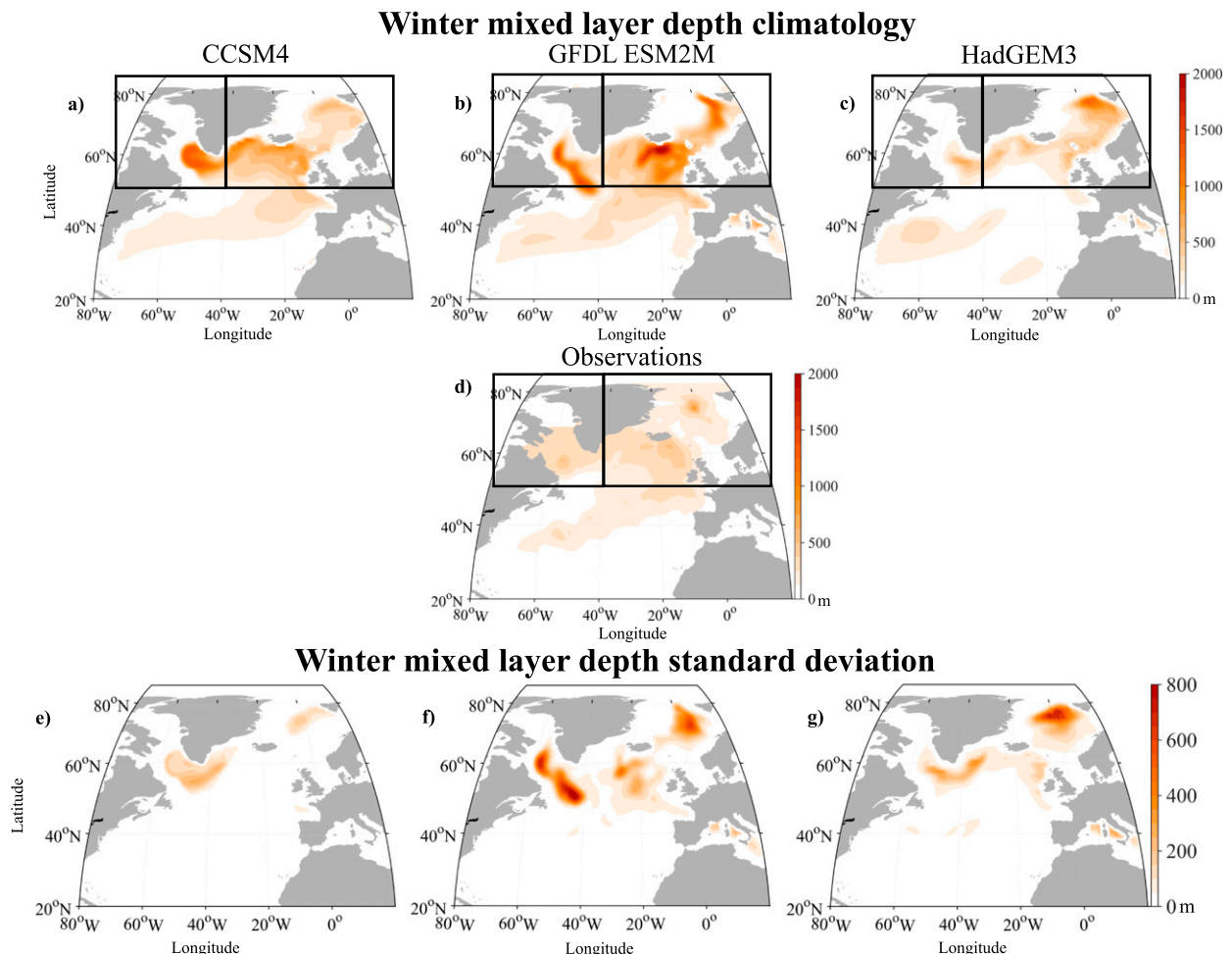## Winter mixed layer depth standard deviation

FIG. 1. (top) Climatology of winter mixed layer depth averaged over January, February, and March for (a) CCSM4, (b) GFDL-ESM2M, (c) HadGEM3, and (d) an observation-based dataset from 1961 to 2008 (de Boyer Montégut et al. 2004, 2007; Mignot et al. 2007). (bottom) Standard deviation of 10-yr low-pass filtered winter mixed layer depth for (e) CCSM4, (f) GFDL-ESM2M, and (g) HadGEM3. Although not shown on the map, the eastern North Atlantic (right) box also includes the area between 20° and 40°E.

gas and aerosol levels, with no volcanic eruptions. We chose these three GCMs for several reasons. First, AMOC and Atlantic OHT variability have been extensively documented within each GCM (Danabasoglu et al. 2012b; Dunne et al. 2012; MacMartin et al. 2013; Msadek et al. 2013; Zhang and Wang 2013; MacMartin et al. 2016; Kuhlbrodt et al. 2018; Menary et al. 2018; Docquier et al. 2019; Li et al. 2019; Jackson et al. 2020; Koenigk et al. 2020; Roberts et al. 2020). Second, they comprise three distinct and commonly used ocean model components: CCSM4 uses the Parallel Ocean Program version 2 (POP2), GFDL-ESM2M uses the Modular Ocean Model version 4p1 (MOM4p1), and HadGEM3 uses the Nucleus for European Modeling of the Ocean version 3.6 (NEMO3.6). Finally, as noted above, the three models differ substantially in their locations of deep convection: CCSM4 shows deep convection primarily in the Labrador Sea, ESM2M shows deep convection primarily in the Irminger and Iceland Basins, and HadGEM3 shows deep convection primarily in the GIN Seas (Figs. 1a–c).

These simulations all have small trends in sea surface temperature, salinity, and potential density. North Atlantic SST trends are on the order of $\sim 1 \times 10^{-3}\,°\mathrm{C\,yr^{-1}}$ or less. North Atlantic sea surface salinity trends are on the order of $\sim 1\text{–}5 \times 10^{-4}\,\mathrm{g\,kg^{-1}\,yr^{-1}}$. North Atlantic sea surface density trends are on the order of $\sim 1\text{–}4 \times 10^{-4}\,\mathrm{kg\,m^{-3}\,yr^{-1}}$. We remove the linear trends from all quantities prior to analysis.

b. Atlantic OHT and mixed layer depth

A comparison of the model climatologies of the ocean circulation and density structure along with the OHT gives context for the analysis of the variability. First, we consider the Atlantic OHT. The climatological Atlantic OHT is similar in all three GCMs, with a peak at around 20°N (Figs. 2a–c), although the magnitude of the peak varies between them, with CCSM4 having the largest peak OHT and HadGEM3 having the smallest. For all of the models, the ocean model grid is rectilinear in the southern part of our analysis domain, but not in the northern part. For CCSM4 and HadGEM3, the true
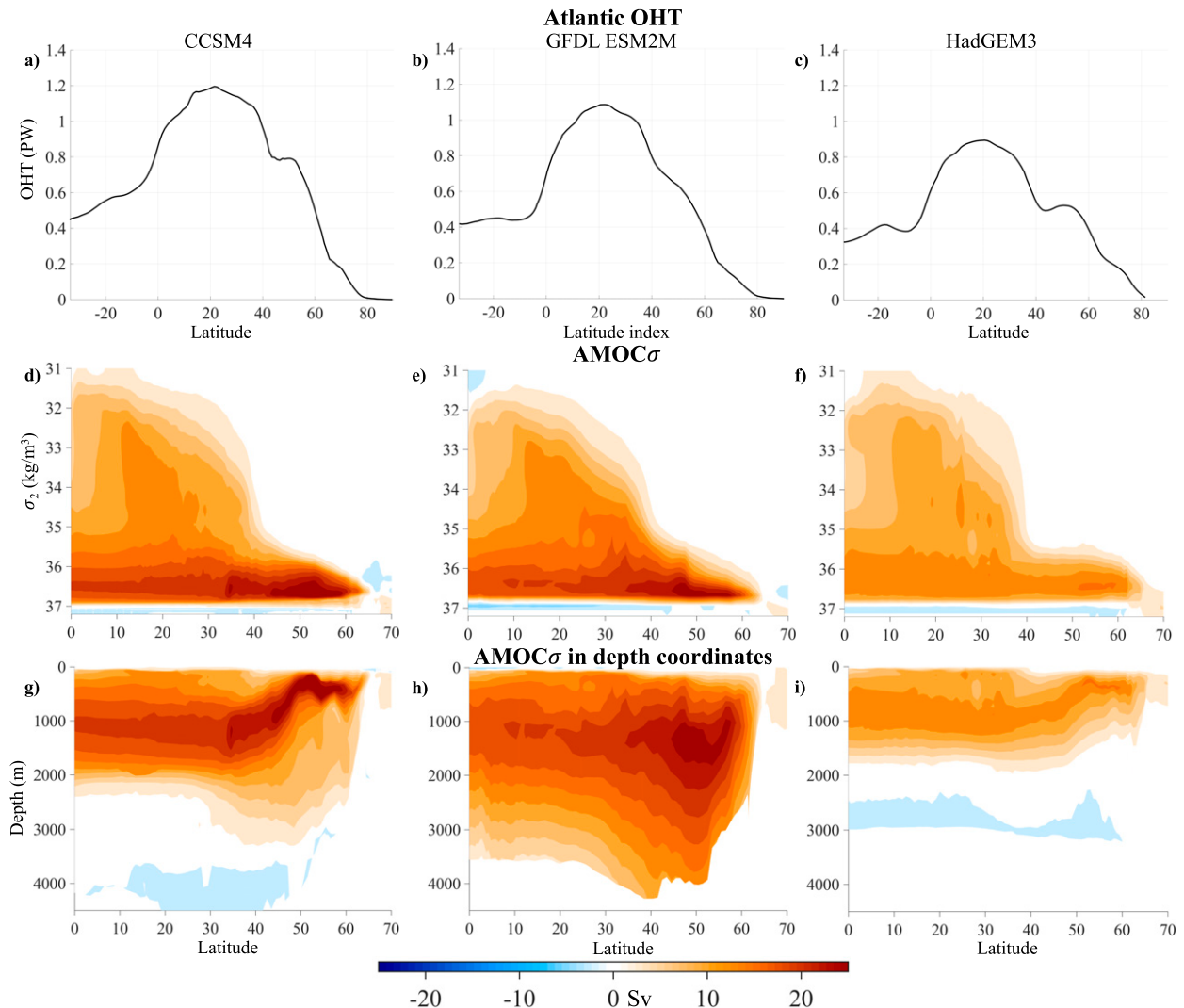
FIG. 2. Climatological fields in (left) CCSM4, (center) GFDL-ESM2M, and (right) HadGEM3: (a)–(c) Atlantic OHT, (d)–(f) AMOCσ, and (g)–(i) AMOCσ remapped to depth coordinates. This mapping is done by calculating the time-mean depth of each isopycnal.

meridional OHT is calculated during run time and is provided as saved monthly fields. However, for GFDL-ESM2M, the OHT on the native grid is provided as saved output. Because the grid in this model is rectilinear south of 65°N, this gives an accurate estimate throughout most of our study region.

We also analyze the winter mixed layer depth (MLD) climatologies, which indicate the regions where the deep convection is concentrated in each model. MLDs are calculated during run time based on the vertical structure of density in the upper ocean (Levitus 1983; Large et al. 1994). The winter MLD climatologies vary considerably between the three GCMs. In CCSM4, the winter mixed layers are deepest in the Labrador Sea, with some deep mixed layers in the Iceland and Irminger Basins as well (Fig. 1a). In GFDL-ESM2M, mixed layers are deeper than in CCSM4, and the deepest mixed layers are located in the Iceland and Irminger Basins, although there is a small band of deep mixed layers in the Labrador Sea (Fig. 1b). In HadGEM3, mixed

layers are the shallowest of all the models, and the deepest mixed layers are located in the GIN Seas (Fig. 1c). Given that we are interested in low-frequency variability, we also look at the standard deviation of the 10-year low-pass filtered winter MLD for each model. In CCSM4, the low-frequency variability is almost entirely concentrated in the Labrador Sea, with a small patch of strong variability in the GIN Seas (Fig. 1e). Although there is strong climatological deep convection in the Irminger and Iceland Basins in this model, there appears to be very little low-frequency variability there. In GFDL-ESM2M, the variability pattern looks somewhat similar to the climatological MLD pattern, but strong variability is more concentrated in the Labrador Sea than climatological deep mixed layers (Fig. 1f). Also, low-frequency variability is overall much stronger than in CCSM4. In HadGEM3, the pattern of low-frequency variability is similar to the climatological MLD pattern, with largest values in the GIN Seas (Fig. 1g).

For comparison, we also include winter MLD climatology computed from observation based datasets from 1961 to 2008 (Fig. 1d) (de Boyer Montégut et al. 2004, 2007; Mignot et al. 2007). In this dataset, deep convection seems to be essentially evenly distributed between the Labrador Sea, the Irminger and Iceland Basins, and the GIN Seas. The observed MLD pattern looks like a combination of the three model climatologies, with somewhat deep mixed layers in all three regions, although the deep mixed layers in the models are not seen in the observations.

c. AMOC in density space

The meridional overturning streamfunction can be calculated in both density space (AMOCσ) and depth space (AMOCz). In density space, AMOCσ shows a maximum in the subpolar region (Figs. 2d–f) because north of 45°N the steep isopycnals below 200 m depth are nearly perpendicular to the isobars. In the subpolar latitudes, there is an extremely large gradient in the overturning streamfunction across a very narrow density range, which represents the North Atlantic Deep Water (NADW) southward deep flow moving along the steep isopycnals. This maximum in overturning is not visible in depth space, because in the subpolar gyre region the northward transport in the east is compensated by southward transport in the west within the same depth layer (Zhang 2010). In AMOCz, strong recirculation south of NADW regions yields a maximum in the midlatitudes instead. Thus, AMOCσ is more appropriate for analyzing subpolar AMOC variability and also allows a focus on the evolution of water mass properties as a function of latitude better than AMOCz (Straneo 2006b; Pickart and Spall 2007).

AMOCσ in density space (henceforth simply referred to as AMOC) is calculated using the following equation:

$$ \text{AMOC}(\sigma, y, t) = -\int_{x_W}^{x_E} \int_{-B(x,y)}^{z(x,y,\sigma,t)} \upsilon(x,y,z,t)\, dz\, dx, \quad (1) $$

where σ is the potential density referenced to 2000 m, y is the latitude, x is longitude, x_W and x_E are the western and eastern longitudinal limits of the basin, respectively, υ is the meridional velocity, z is depth (positive upward), $B(x,y)$ is the bottom depth, and t is time. For CCSM4, we do this calculation using monthly model output velocity data. For GFDL-ESM2M and HadGEM3, we use model output of the AMOC.

The relative strength of AMOC and the density class where AMOC reaches its maximum for each model will become relevant when we discuss the regressions of AMOC and the WMT onto the first LFC of OHT. The AMOC climatologies for CCSM4 and ESM2M are similar, although ESM2M's is weaker, and its maximum is shifted toward lower latitudes and slightly lighter densities (Figs. 2d,e). CCSM4's AMOC maximum of 29.1 Sv (1 Sv $\equiv 10^6$ m^3 s^{-1}) is located at 52.2°N and $\sigma_2 = 36.69$ kg m^{-3}. ESM2M's AMOC maximum of 27.4 Sv is located at 47.5°N and $\sigma = 36.6$ kg m^{-3} (Figs. 2d,e). HadGEM3's AMOC maximum of 15.4 Sv, which is much weaker than that in CCSM4 or ESM2M, is located at 52.3°N and $\sigma_2 = 36.5$ kg m^{-3} (Figs. 2f,i). The vertical structure is substantially different between the models as well (Figs. 2g–i).

In CCSM4 and HadGEM3, AMOC shoals with latitude and the maximum AMOC is at a shallower depth than in GFDL-ESM2M, where the overturning streamfunction actually deepens with latitude.

d. Surface-forced water mass transformation and overturning streamfunction

The surface-forced WMT quantifies the density flux into the ocean due to surface buoyancy forcing (i.e., air–sea heat and freshwater fluxes). It also links changes in surface fluxes and winds in different regions to changes in AMOC (Langehaug et al. 2012b). WMT is calculated from air–sea heat and freshwater fluxes (Tziperman 1986; Speer and Tziperman 1992; Langehaug et al. 2012b). Mixing also provides a substantial contribution to WMT (Nurser et al. 1999), often opposing the surface-forced WMT in the North Atlantic (Tandon and Zhao 2004), though it is generally much weaker than the surface-forced component outside of the tropics. Nurser et al. (1999) used a coupled model and estimated the magnitude of the total mixing component to be about 4 Sv in the subpolar North Atlantic, or about 40% as large as the surface-forced component. Here we neglect this contribution as the publicly available model data do not have sufficient time resolution to examine the mixing component in these models.

Our WMT calculation follows the methods of Speer and Tziperman (1992). The surface density flux $D(x, y, t)$ is calculated via

$$ D(x,y,t) = \frac{\alpha(x,y,t)Q_H(x,y,t)}{c_w} - \beta(x,y,t)S(x,y,t)Q_F(x,y,t), \quad (2) $$

where the first and second terms are the heat and freshwater flux components (kg m^{-2} s^{-1}), respectively; $\alpha(x, y, t)$ is the thermal expansion coefficient calculated at each grid point for every month of output data; Q_H is the surface heat flux into the ocean (W m^{-2}); c_w is the specific heat capacity of seawater, assumed to be uniform and constant with a value of 4186 J kg^{-1} K^{-1}; $\beta(x, y, t)$ is the haline contraction coefficient also calculated at each grid point for each time step; S is the surface absolute salinity; and Q_F is the freshwater flux (kg m^{-2} s^{-1}). The surface heat flux includes contributions from latent and sensible heat fluxes, net shortwave and longwave radiation fluxes, and heat fluxes from sea ice changes. The freshwater flux is the sum of the precipitation, evaporation, runoff, and sea ice formation and melt fluxes. All quantities listed here are either from monthly model output data or calculated using monthly data. The $D(x, y, t)$ model climatologies are shown in Figs. 3a–c.

The surface-forced WMT at each density is calculated by integrating $D(x, y, t)$ over all surface area in each density bin:

$$ F(\sigma) = \frac{1}{\Delta\sigma} \iint_{\sigma}^{\sigma+\Delta\sigma} D(x,y,t)\, dA, \quad (3) $$

where $F(\sigma)$ is the surface forced WMT (Sv), $\sigma = \rho - 1000$ is the potential density referenced to 2000 m (kg m^{-3}), and $\Delta\sigma$ is the width of each density bin.
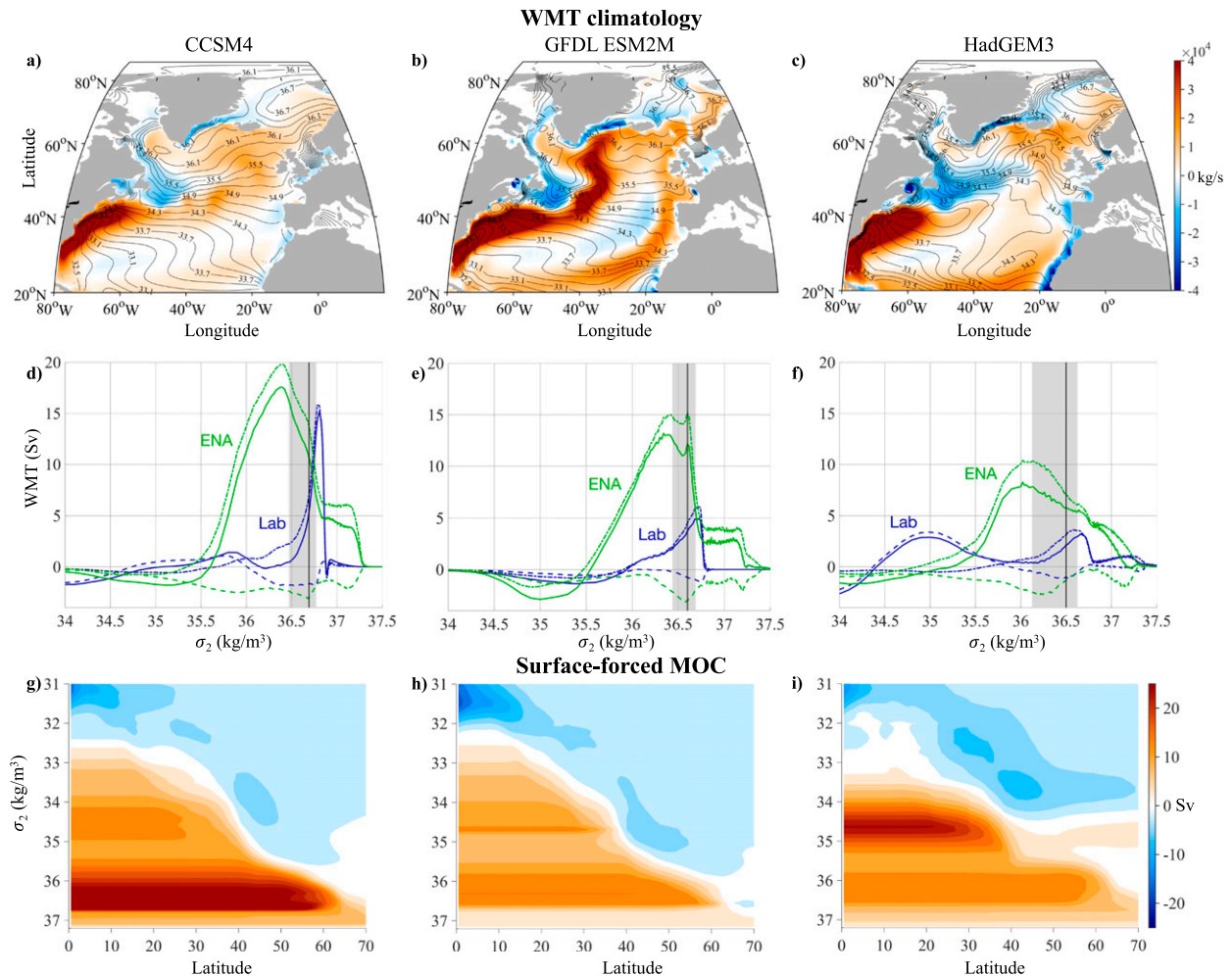
WMT climatology

FIG. 3. Climatological fields in (left) CCSM4, (center) GFDL-ESM2M, and (right) HadGEM3. (a)–(c) Total surface density flux $D(x, y, t)$, calculated using Eq. (2). (d)–(f) Water mass transformation thermal (dot-dashed lines), freshwater (dashed lines), and total (solid lines) components in the Labrador Sea and the eastern North Atlantic (ENA). The black vertical lines indicate the density where the climatological AMOCσ reaches its maximum in each model. The gray shaded areas represent the density range where AMOCσ is within 10% of its maximum value. (g)–(i) Surface-forced overturning streamfunction in density coordinates.

We also examine the total $F(\sigma)$ in regions that encompass the Labrador Sea separately from the GIN Seas and Irminger and Iceland Basins (for the location of these regions, see the marked boxes in Fig. 1). Here, we include both the GIN Seas and the Iceland and Irminger Basins in one box which we call the eastern North Atlantic (ENA) region in order to include all surface density fluxes east of the Labrador Sea. We use potential density referenced to 2000 m to allow for easier comparison with AMOC, which is typically computed using σ_{2000}. We have also carried out our analysis using σ_0 and this did not substantially change our results.

The partitioning of climatological WMT between the Labrador Sea and the ENA differs substantially among the models (Figs. 3d–f). Because models with a greater proportion of WMT in a particular high-latitude deepwater formation region also have deep mixed layers there, it is possible to identify where high-latitude WMT is concentrated by looking

at MLD. In CCSM4, because there are large areas with deep mixed layers not only in the Labrador Sea but also in the Iceland and Irminger Basins, both the Labrador Sea and ENA contribute substantially to the WMT within the density range where AMOC is at or near its maximum (Fig. 3d). For both ESM2M and HadGEM3, the ENA dominates the WMT at all density classes that outcrop in the models' deepwater formation regions (i.e., the regions with the deepest mixed layers). In all three models, the thermal WMT component dominates over the haline component. The haline component provides a substantial opposing contribution in both the Labrador Sea and ENA in the density range where AMOC is at its maximum (Figs. 3d–f). The haline component of WMT is most important in HadGEM3 and least important in GFDL-ESM2M (Figs. 3e,f). We compare the WMT computed from the models to what is found in observational datasets in section 3 below.

TABLE 1. Absolute value of the bias between modeled or convolved model-observational WMT components and observation-based WMT components for CCSM4, GFDLESM2M, and HadGEM3 in the Labrador Sea and ENA regions. Each number represents the absolute value of the difference between the convolved WMT and the WMT computed from observation-based data (in Sv).

	Thermal/Labrador	Freshwater/Labrador	Thermal/ENA	Freshwater/ENA
CCSM4/CCSM4	0.94	3.76	0.65	1.86
GFDL-ESM2M/GFDL-ESM2M	0.96	0.54	1.76	0.86
HadGEM3/HadGEM3	0.76	0.45	1.00	0.64
OAFlux/ERA5/CCSM4	0.88	0.23	0.83	0.17
OAFlux/ERA5/GFDL-ESM2M	0.82	0.28	1.4	0.23
OAFlux/ERA5/HadGEM3	0.47	0.25	1.40	0.40
CCSM4/EN4/OISST	1.12	0.61	2.98	0.88
GFDL-ESM2M/EN4/OISST	0.47	0.22	1.58	0.67
HadGEM3/EN4/OISST	0.29	0.21	1.72	1.02

To understand how much of the structure of AMOC in latitude and density can be attributed to WMT, we compare the full AMOC from Eq. (1) against the surface-forced overturning streamfunction (as a function of latitude rather than in specific regions) calculated following Marsh (2000). The surface-forced MOC $F(\sigma, \Theta, t)$ is calculated from the divergence of the surface density flux:

$$F(\sigma, \Theta, t) = -\frac{\partial}{\partial \sigma} \iint_{\theta > \Theta, \sigma^* > \sigma} D(x, y, t)\, dA, \qquad (4)$$

where σ is the surface density; σ^* is a dummy variable representing surface density; Θ is the latitude; θ is a dummy variable representing latitude; $D(x, y, t)$ is the density flux given by Eq. (2); t is the time; and A is the surface area.

In both CCSM4 and ESM2M, there is a substantial discrepancy between the climatological surface-forced overturning streamfunction and the climatological full AMOC streamfunction (Figs. 3g,h; cf. Figs. 2d,e), which can be attributed to mixing. The maximum surface-forced MOC across all densities and all latitudes north of 35°N is equal to 32.9 and 15.0 Sv for CCSM4 and ESM2M, respectively (Figs. 3g,h), whereas the maximum AMOC is equal to 29.9 and 27.4 Sv, respectively (Figs. 2d,e). In CCSM4, the mixing contribution to overturning is small, about 10% as large as the surface-forced term, and acts to weaken the overturning. In ESM2M, the mixing term is more substantial, about 45% as large as the surface-forced contribution, and acts to strengthen overturning. Substantial discrepancies between the surface-forced MOC and the total AMOC are not uncommon in models; discrepancies greater than 15 Sv have been found in some models (Grist et al. 2009). The surface-forced AMOC is typically stronger than the total AMOC, but the reverse has been found in at least one model (Grist et al. 2009).

In HadGEM3, the surface-forced overturning streamfunction and full AMOC are similar in magnitude (Figs. 2f and 3i). The maximum surface-forced MOC across all densities and all latitudes north of 35°N is equal to 15.6 Sv (Fig. 3i), and the maximum AMOC is equal to 15.4 Sv (Fig. 2f) such that there is a very small mixing contribution in this model, about 1% as large as the surface-forced component. However, mixing weakens the MOC substantially in denser layers (Figs. 2f and 3i).

Our results are somewhat similar to what was found in an analysis of a high-resolution model (Xu et al. 2018), which noted a substantial discrepancy between the total and surface-forced overturning streamfunctions.

3. Comparison of model water mass transformation to observational datasets

To determine how realistic the representation of surface WMT is in each of the GCMs, we compare with WMT computed from oceanic and atmospheric observation-based datasets. We further consider whether model biases in sea surface temperature, salinity, or air–sea surface fluxes are responsible for any discrepancies in WMT between the models and observations. To do so, we use monthly surface air–sea heat fluxes over the 26-yr period 1984–2009 from the Objectively Analyzed Air–Sea Fluxes dataset (OAFlux; Yu et al. 2008), monthly SSTs from NOAA Optimum Interpolation Sea Surface Temperature V2 (OISST; Reynolds et al. 2002) and surface salinities from the Hadley Centre's EN4.2.1 (Good et al. 2013). Using SST data from EN4.2.1 instead of OISST does not substantially change the results. To estimate freshwater fluxes, we use monthly precipitation, evaporation, snowmelt, and river runoff data from the ECMWF atmospheric reanalysis (ERA5; Hersbach and Dee 2016). Precipitation and evaporation are taken directly from ERA5 monthly averaged output, while river runoff is calculated by routing net precipitation over land (from ERA5) to the appropriate ocean grid point using the STN30p River Topology dataset (Vörösmarty et al. 2000), as described in Wills and Schneider (2015).

We convolve the monthly observed surface fluxes with SSTs and surface salinities from the equivalent years (1984–2009) of OISST and EN4.2.1 to calculate the WMT and compare that to the WMT in models. We then swap out the observed sea surface temperature and salinity for those fields taken from each of the models, comparing the resulting WMT with that derived from observations. Similarly, we repeat the calculation using observed sea surface temperature and salinity fields but with the observed surface fluxes swapped for modeled fluxes. In Table 1, we provide the absolute value difference between the convolved WMT and the observation-based WMT averaged over the density range $35\,\mathrm{kg\,m^{-3}} < \sigma_2 < 37.3\,\mathrm{kg\,m^{-3}}$. We choose this density range because it is the range of peak

AMOC. Although we use data from preindustrial control simulations in this analysis, we have also done the same calculations using historical simulation data and found similar results.

Similar to the models, the observation-based WMT shows positive values in the Labrador Sea as well as the ENA. In both of these regions, strong, sustained winter heat loss to the atmosphere overwhelms any compensating effects from freshwater fluxes (Fig. 4). The ENA dominates the WMT at densities above approximately $35.8 \, kg \, m^{-3}$. The freshwater components in both regions are negative, with a small but nonnegligible magnitude corresponding to approximately 17% of that of the thermal component in the Labrador Sea and 22% in the ENA. The WMT in the two regions occur over a larger range of densities compared to the WMT in models (Figs. 4 and 3d–f). Of the three models, HadGEM3 is the most similar to observations (cf. Fig. 3f).

To examine what features of the models control the differences with observations, we first convolve observation-based sea surface temperatures and salinities with surface fluxes from the different models. Swapping out the observed surface heat and freshwater fluxes for CCSM4's results in a large increase in the magnitude of the thermal WMT component in the ENA, and a smaller increase in the Labrador Sea (Fig. 5d). The magnitude of the freshwater component becomes substantially larger in both regions as well. Swapping out the observed surface heat and freshwater fluxes for ESM2M's yields a result that is closer to the WMT computed from observations than CCSM4 (Fig. 5e). Finally, swapping in HadGEM3's surface fluxes results in a WMT that is closest to observations in the Labrador Sea, but slightly worse than GFDL-ESM2M in the ENA (Fig. 5f).

Convolving the observed surface fluxes with CCMS4 SST and surface salinities causes the Labrador Sea WMT to be concentrated over a smaller density range and at a higher density class, and also yields substantially stronger thermal WMT in the ENA (Fig. 5a). Swapping out the observed SSTs and salinities for ESM2M's causes both the Labrador Sea and ENA WMT to be concentrated over smaller density ranges, with large, narrower peaks at $\sigma_2 = 36.6$ and $\sigma_2 = 36.7$, respectively. This ENA WMT is less similar to observations than CCSM4 (Fig. 5b). In the Labrador Sea, the result is not substantially closer to or farther from observations (Fig. 5b). Swapping out the observed SSTs and salinities for HadGEM3's in the Labrador Sea gives a result that is the most similar to what is found when using observational data (Fig. 5c), In the ENA, HadGEM3 performs worse than CCSM4 when averaged over the entire density range. However, the full pattern actually looks more similar to observations than the other two models (Fig. 5c). The freshwater WMT component becomes slightly smaller when using sea surface temperatures and salinities from models, particularly when using GFDL-ESM2M and HadGEM3 SSTs and salinities.

Based on these results, it appears that in the ENA biases in surface heat and freshwater fluxes are largely responsible for the discrepancy between WMT calculated from models and from observational data; biases in sea surface temperatures and salinities play a secondary role. However, in the Labrador Sea, it seems that biases in sea surface temperatures and
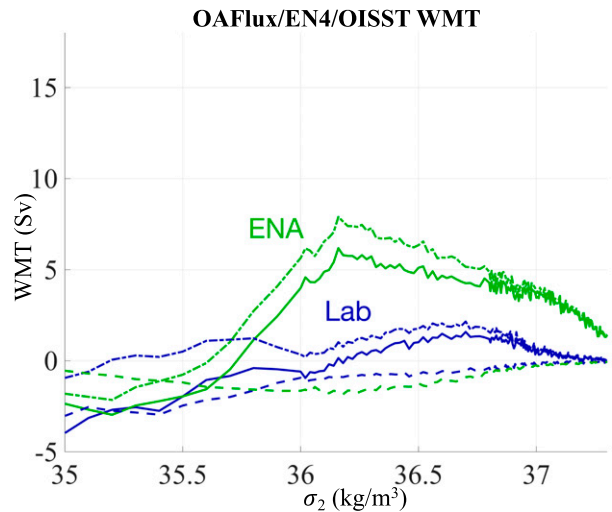

FIG. 4. Water mass transformation thermal (dot-dashed lines), freshwater (dashed lines), and total (solid lines) components integrated over the Labrador Sea and ENA boxes using OAFlux surface heat fluxes and ERA5 freshwater fluxes convolved with OISST SSTs and EN4.2.1 surface salinities.

salinities are more responsible for the discrepancy. Although HadGEM3 is the most realistic of all the models in both its surface fluxes and surface temperatures and salinities, particularly in the Labrador Sea, it still has substantial biases in surface fluxes relative to observations, especially in the ENA. This will be important to keep in mind when we consider the role of WMT variability in low-frequency OHT variability in these models in the following section.

4. Mechanisms of low-frequency OHT variability

To examine the controls on low-frequency OHT variability, we first apply a low-frequency component analysis (LFCA; Wills et al. 2018, 2019a) to Atlantic OHT in all three GCMs. We solve for the low-frequency patterns (LFPs) of the OHT, which are the linear combinations of the leading empirical orthogonal functions (EOFs) that maximize the ratio of low-frequency variance to total variance in their corresponding time series [called low-frequency components (LFCs)]. Low-frequency variance is defined as the variance that remains after the application of a Lanczos filter with a low-pass cutoff of 10 years. The 10-yr low-pass filter is only used in identifying the LFPs, and all information about high-frequency variations in the data is preserved. LFCA is related to a broader class of statistical analyses that identify patterns that maximize the ratio of signal to noise (Allen and Smith 1997; Venzke et al. 1999; Schneider and Griffies 1999; Schneider and Held 2001; Ting et al. 2009). We focus on the first LFP/LFC (Figs. 6a–c,g–i), which has the highest ratio of low-frequency variance to total variance and is well separated in this ratio from the second LFP/LFC. This LFP represents the Atlantic OHT anomaly associated with a one standard deviation (1σ) anomaly in the corresponding LFC time series. When calculating the LFPs/LFCs for CCSM4 and HadGEM3,
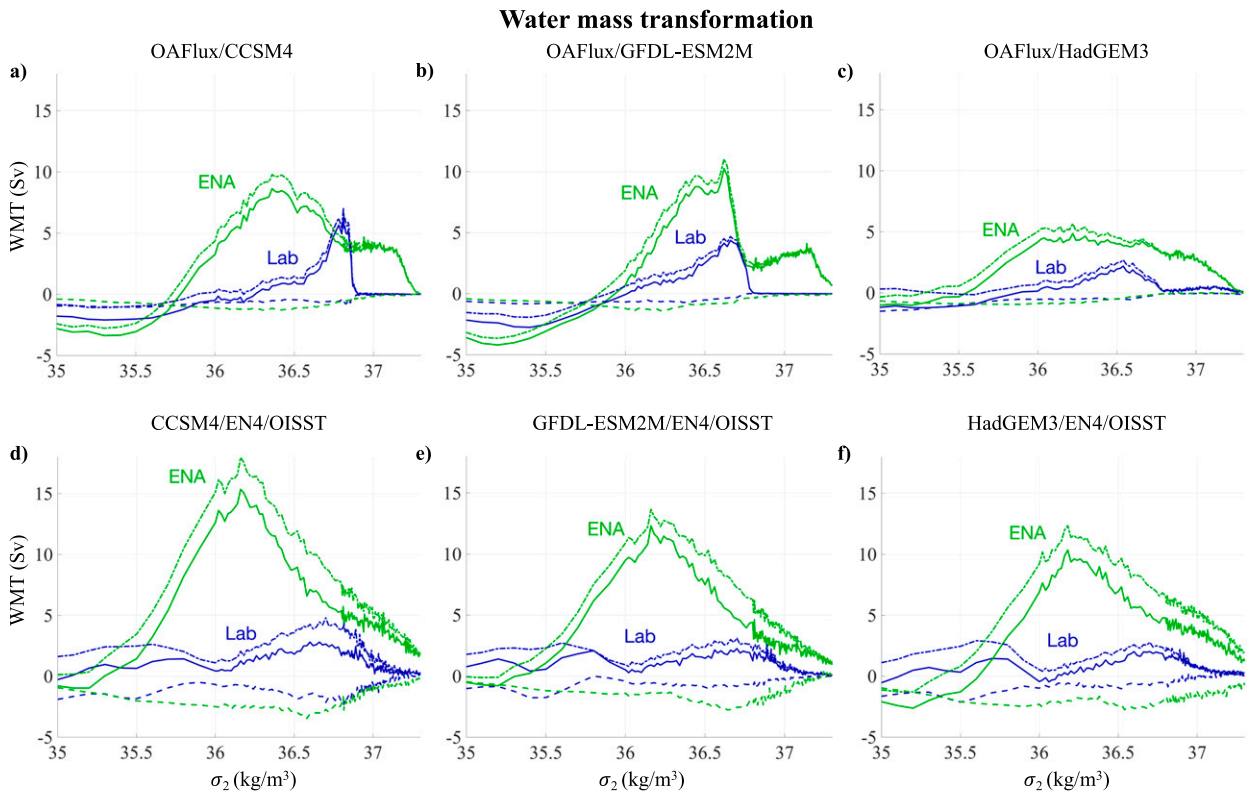
Water mass transformation

FIG. 5. Water mass transformation thermal (dot-dashed lines), freshwater (dashed lines), and total (solid lines) components integrated over the Labrador Sea and ENA boxes. (top) WMT calculated using OAFlux surface heat fluxes and ERA5 freshwater fluxes convolved with sea surface temperatures and salinities from (a) CCSM4, (b) GFDL-ESM2M, and (c) HadGEM3. (bottom) WMT calculated using OISST SSTs and EN4.2.1 surface salinities convolved with surface heat and freshwater fluxes from (d) CCSM4, (e) GFDL-ESM2M, and (f) HadGEM3.

we include the six leading EOFs (92.8% and 93.1% of the total variance, respectively). For GFDL-ESM2M, we include the seven leading EOFs (96.5% of the total variance). The choice of the number of EOFs does not substantially change the results for any of the models.

A traditional approach to studying AMOC variability is to composite on indices such as the AMOC index (Delworth et al. 1993; Danabasoglu et al. 2012b; Langehaug et al. 2012b; Tulloch and Marshall 2012; MacMartin et al. 2013), defined as the normalized maximum value of the meridional overturning streamfunction in density coordinates across all densities and latitudes north of 35°N, or a convective index, defined as the normalized density anomaly averaged over the models' respective deep convection regions. However, those indices explain a smaller fraction of low-frequency OHT variance than does the first LFC (Figs. 6d–f), and also have a smaller signal-to-noise ratio. Another commonly used metric, the first principal component of the low-pass filtered OHT, explains a similar amount of low-frequency variance (Figs. 6d–f); however, the loss of time resolution makes it difficult to discern lead–lag relationships (Cane et al. 2017; Wills et al. 2019a), precluding a full mechanistic understanding of the drivers of OHT changes, particularly the role of processes occurring on shorter time scales. To determine the mechanisms driving

low-frequency OHT variability, we compute lead–lag regressions of anomalies in several atmospheric and ocean fields onto the LFC: upper ocean density, SLP, ocean heat content, winter MLD, the barotropic streamfunction, AMOC, and WMT. We calculate the statistical significance of each regression using 500 phase randomized samples of the LFC (Ebisuzaki 1997). The salient features of all regressions are statistically significant at the 95% level. Plots of statistical significance are included here for winter MLD (Fig. 10) and upper-ocean density (Fig. 13).

Although high-frequency variability (in, for example, WMT) does not necessarily affect AMOC and OHT, only variability associated with low-frequency changes in AMOC and OHT would show up in the regressions, because the variables are regressed onto the LFC. Other unrelated high-frequency variability would not be correlated with the LFC because the LFC has very little high-frequency variability.

a. The pattern of low-frequency Atlantic OHT variability

The first LFPs of CCSM4 and GFDL-ESM2M are similar in that they are both meridionally coherent with a narrow peak in the midlatitudes around 45°N (Figs. 6a,b). The main difference is that GFDL-ESM2M's LFP has a higher magnitude owing to stronger AMOC variability in that model (Yan et al. 2018). For HadGEM3, the magnitude of the first LFP of OHT is smaller
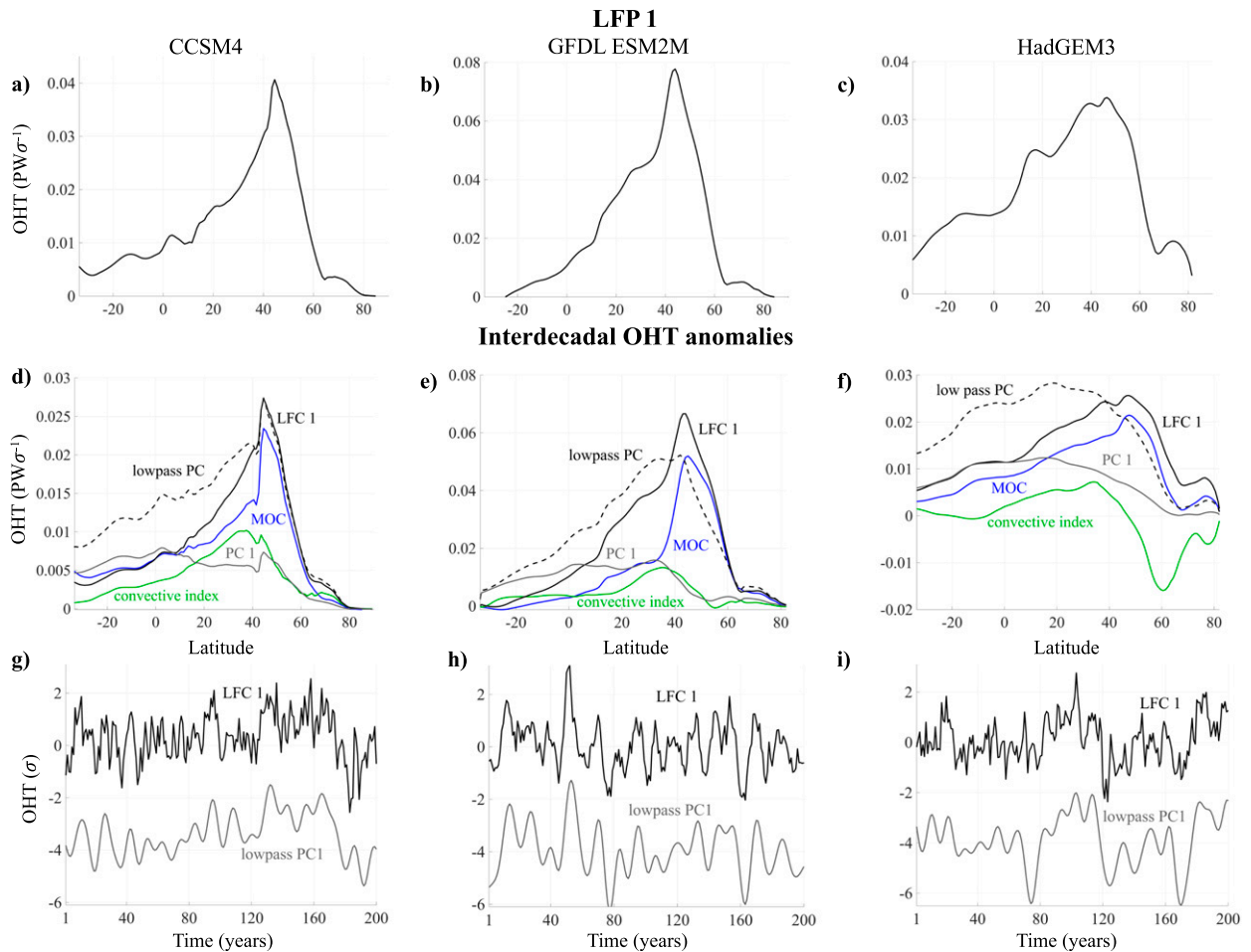
LFP 1

FIG. 6. (top) First LFP of Atlantic OHT for (a) CCSM4, (b) GFDL-ESM2M, and (c) HadGEM3. (middle) Regressions of 10-yr low-pass filtered Atlantic OHT on different indices in units of PW per standard deviation of the index for (d) CCSM4, (e) GFDL-ESM2M, and (f) HadGEM3. The AMOC index is the normalized maximum value of the meridional overturning streamfunction in density coordinates across all densities and latitudes north of 35°N. The convective index is the normalized density anomaly in the models' respective convective regions, excluding grid cells with winter MLD < 500 m for CCSM4, winter MLD < 700 m for GFDL-ESM2M, and winter MLD < 400 m for HadGEM3. PC1 represents the first principal component of the OHT. Low-pass PC1 is the first principal component of the 10-yr low-pass filtered OHT. (bottom) Time series for both LFC 1 and the low-pass PC1 for (g) CCSM4, (h) GFDL-ESM2M, and (i) HadGEM3. Low-pass PC1 time series are shifted downward by −4 on the y axis.

than the other two models, with a broader peak in the mid-latitudes (Fig. 6c). The ratios of low-frequency variance to total variance are 0.69, 0.89, and 0.76 for CCSM4, GFDL-ESM2M, and HadGEM3, respectively.

To justify our use of the LFCA as opposed to using a more conventional index, we include here a plot of the regressions of the 10-yr low-pass filtered OHT onto the LFC and other indices, which are a measure of the low-frequency OHT variance explained by the different indices. The regressions indicate that in all three models, the LFC indeed explains more low-frequency OHT variance than other indices, including the first PC of the non-low-pass filtered OHT, the AMOC index, and the convective index (Figs. 6d–f). This indicates that although AMOC plays a major role in low-frequency OHT variability, there are other important processes that contribute

to the variability as well. It is also evident that in CCSM4 and ESM2M, the LFP exhibits a similar pattern to the first PC of the low-pass filtered OHT, with the peaks almost exactly aligned, although it explains less low-frequency variance at some latitudes. In all models, the meridional structure of the LFC is more similar to the structure of the OHT regressed onto the AMOC index than the low-pass PC. The LFP creates an index that yields a similar time series to that of the low-pass PC but with all time resolution left intact; hence, the LFP captures rapid transitions within low-frequency OHT variability (Figs. 6g–i). For HadGEM3, the LFC spatial pattern is different from what is found in the low-pass PC; the peak in the low-pass PC is located farther south than that in the LFP (i.e., at 18.5°N vs 45°N for the LFC; Fig. 6f), possibly because the low-pass PC includes aliasing of higher-frequency subtropical OHT variability.
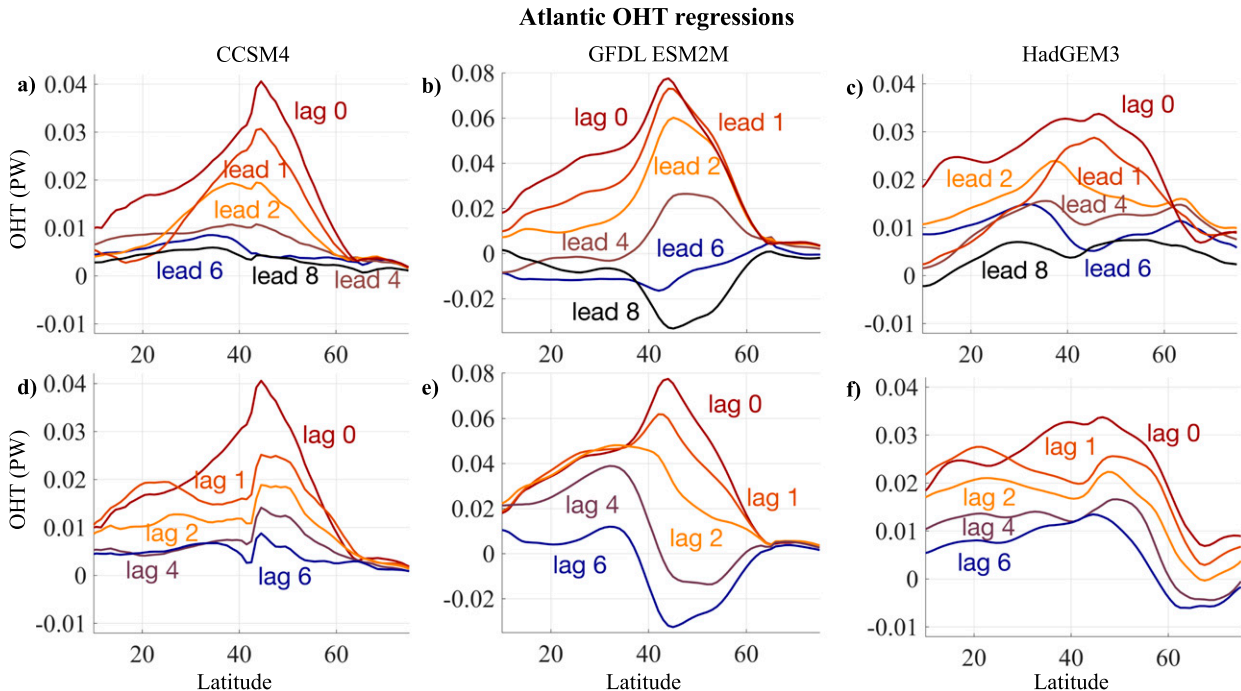
Atlantic OHT regressions

FIG. 7. Lead–lag regressions of OHT onto the first LFC of OHT for (left) CCSM4, (center) GFDL-ESM2M, and (right) HadGEM3: (a)–(c) lead times and (d)–(f) lag times. Lead means LFC 1 lags, i.e., prior to the maximum OHT. Because the LFCs are unitless, the regressions simply have units of PW (per standard deviation).

In other words, sufficiently strong white noise in tropical and subtropical OHT could still be present in low-pass filtered data and shift the maximum in the EOF toward the tropics.

b. Mechanisms of low-frequency OHT variability in CCSM4

To examine the mechanisms that drive low-frequency OHT variability, we next study lead–lag relationships between the first LFC time series and different oceanic and atmospheric variables. We begin by discussing the results for CCSM4 before comparing to the other two models in the subsequent subsections. Lagged regressions of the OHT onto the LFC time series reveals how the OHT pattern progresses leading up to (Fig. 7a) and following (Fig. 7d) the time of maximum OHT, as captured by the LFC. These regressions indicate that at lead times (i.e., prior to the time of maximum OHT), the OHT steadily increases in magnitude before reaching its maximum at lag zero with a peak at 45°N. (Fig. 7a). At lag times (i.e., after the time of maximum OHT), the OHT steadily decreases in magnitude. The OHT spatial pattern at lag times is different from the one at lead times, as there is a large change in gyre circulation after the time of maximum OHT, causing an abrupt jump in OHT at the boundary between the subtropical and subpolar gyres (cf. Fig. 8f).

Lagged regressions between the LFC and winter SLP, as well as the associated wind stress anomalies, reveal the role that atmospheric forcing plays in driving the OHT variability. In the eight years before the time of maximum OHT, there is a persistent SLP pattern associated with anomalous northwesterly winds off eastern North America (Figs. 9a–c show leads up to 6 years). This

pattern is similar to the NAO, but the center of the high pressure system is northwest of where it appears in the NAO SLP pattern in observations. Since the persistence time scale of SLP anomalies is less than one month (Ambaum and Hoskins 2002), the persistence of this pattern must be due to memory in the ocean. In the two years before the time of maximum OHT, this pattern becomes more zonal. At the time of maximum OHT, the eastern part of the high pressure region near western Europe intensifies, while the western part dissipates. This intensification corresponds to Ekman transport that reinforces the low-frequency OHT pattern, which shows up because high-frequency variability is not completely filtered out by the LFCA. This intensification does not occur when the SLP data are low-pass filtered (not shown). Only weak SLP anomalies remain after the maximum OHT (Fig. 9f), indicating a weak atmospheric response to this variability. The anomalous winds at lead times cause mixed layers in the Labrador Sea to deepen by inducing anomalous heat loss to the atmosphere and increasing mixing at the surface (Figs. 10a–c). The mixed layers reach their deepest two years prior to the maximum OHT, and quickly shoal after lead 1 (Figs. 10d–f).

Concurrent with deepening mixed layers in the Labrador Sea, WMT in that region increases, peaking two years before the maximum OHT (Fig. 11a). This increase in WMT is centered around $\sigma_2 = 36.87$, where it reaches a maximum of 2.9 Sv. This is at a somewhat higher density than the density where the AMOC anomaly at lag zero reaches its maximum (Fig. 11a). There is a relatively small change in WMT in the ENA (Fig. 11d), which peaks at $\sigma_2 = 36.74$, with a maximum value of 0.6 Sv. This is a substantially lower density than where the AMOC anomaly reaches
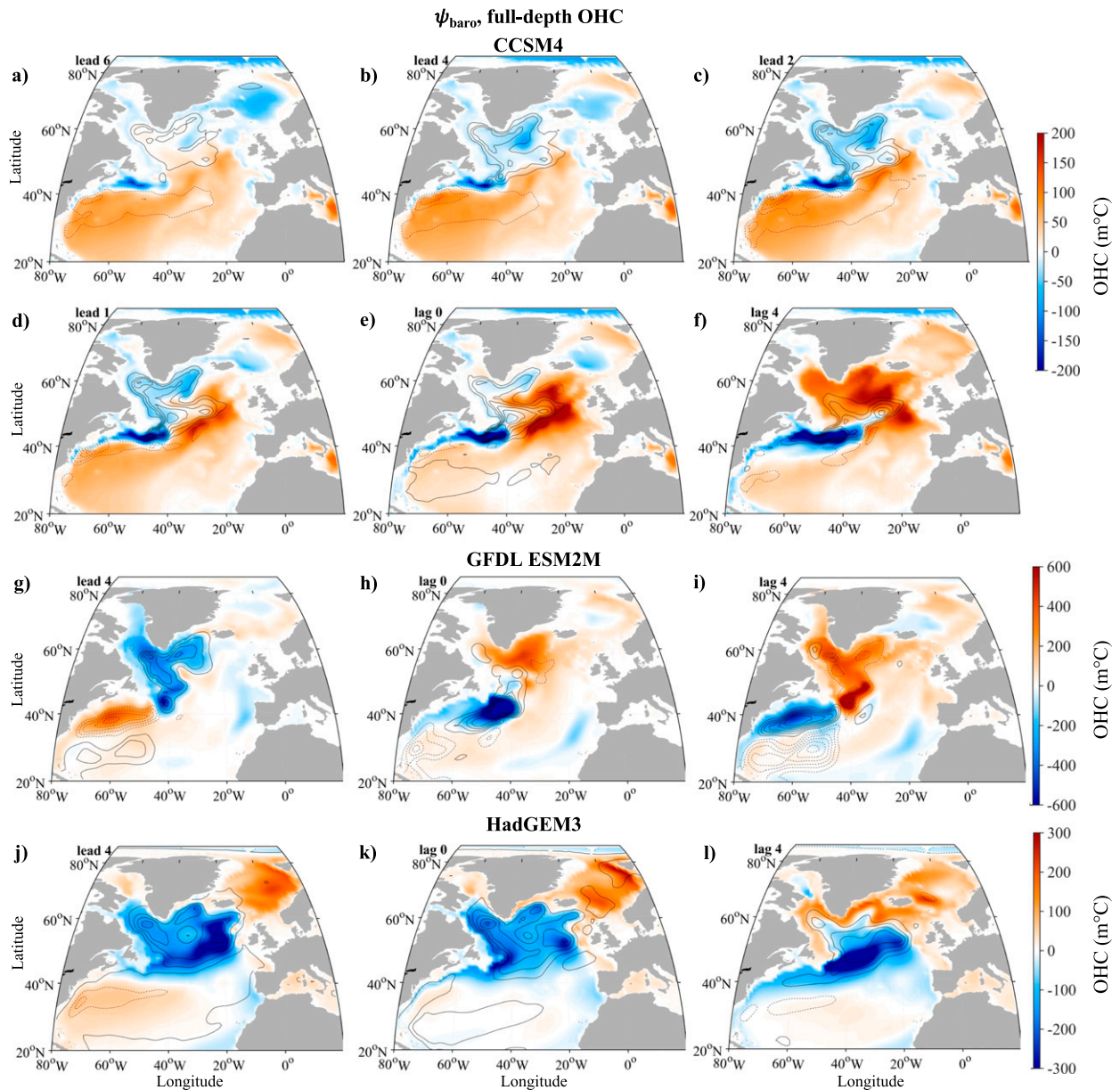
ψ_{baro}, full-depth OHC

FIG. 8. Lead–lag regressions of the barotropic streamfunction (contours) and full-depth ocean heat content (colors) onto the first LFC of OHT for (a)–(f) CCSM4, (g)–(i) GFDL-ESM2M, and (j)–(l) HadGEM3. Barotropic streamfunction contours are spaced every 0.25 Sv for CCSM4 and HadGEM3 and 0.5 Sv for GFDL-ESM2M. Solid lines indicate cyclonic/positive values, and dashed lines indicate anticyclonic/negative values. Lead times indicate anomalies that lead the LFC, i.e., prior to the maximum OHT. Because the LFCs are unitless, the regressions simply have units of Sv and °C m (per standard deviation) for the barotropic streamfunction and OHC, respectively.

its maximum at lag zero, albeit closer to the density of maximum climatological AMOC. The WMT changes are overwhelmingly dominated by heat-flux changes (Figs. 12a,d). After lead 2 years, WMT decreases in both regions as the SLP pattern becomes more zonal at lead 1 before weakening after the time of maximum OHT. It is unclear which density range is most important for AMOC variability, and neither the Labrador Sea nor the ENA WMT peaks align exactly with the peak in the AMOC anomaly (Figs. 11a,d). However, the peak in WMT is generally larger in the

Labrador Sea than the ENA. Moreover, the Labrador Sea peak occurs at higher densities than the AMOC anomaly, which would be consistent with internal mixing acting to lighten the densest water masses. Altogether, this suggests to us that the Labrador Sea primarily drives OHT and AMOC variability in this model, although the ENA may still make an important contribution.

As WMT increases in the Labrador Sea, near-surface Labrador Sea waters cool and densify (Figs. 13a–c), and the increase in WMT and surface density fluxes causes AMOC to strengthen
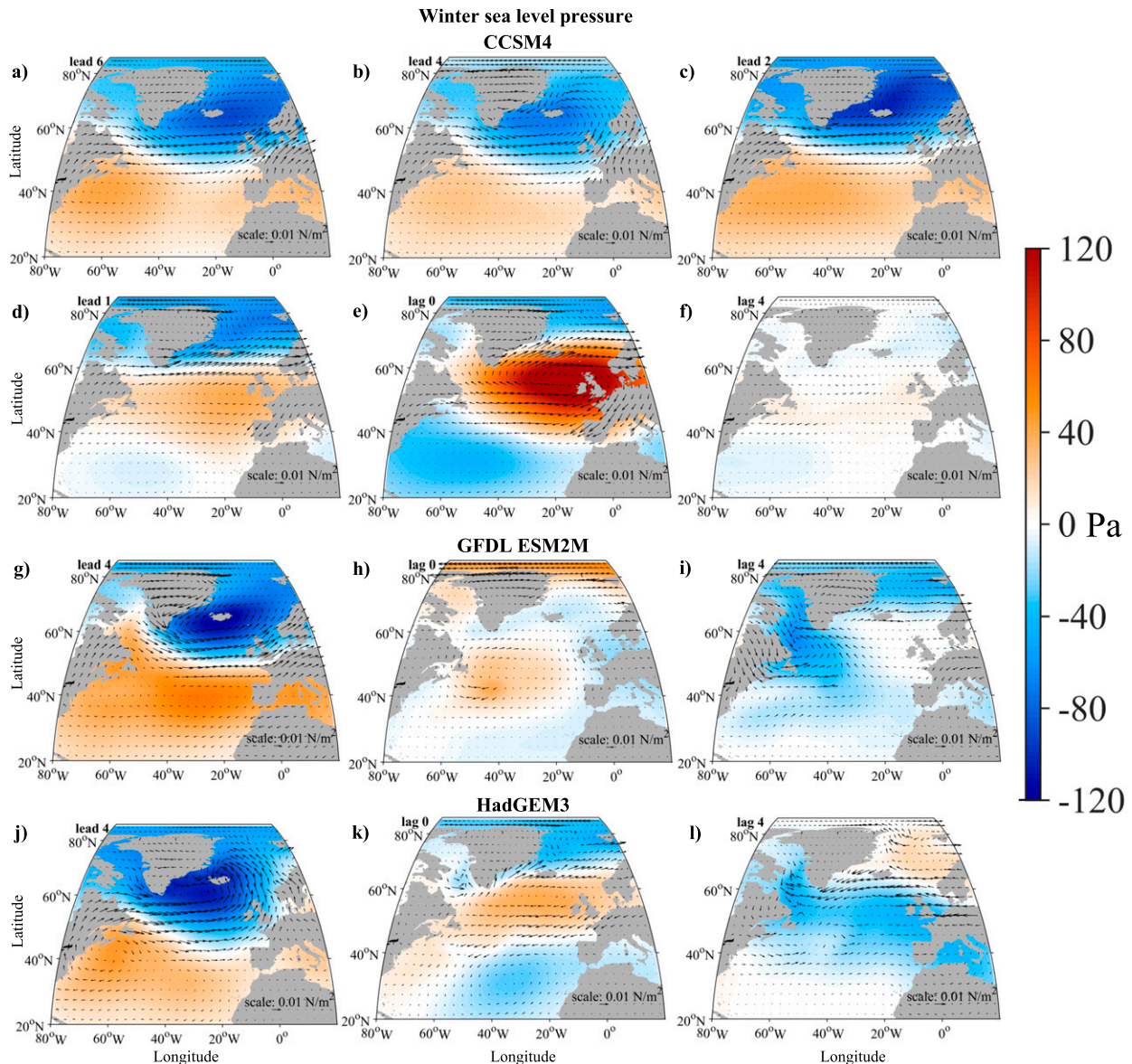
Winter sea level pressure

FIG. 9. Lead–lag regressions of sea level pressure averaged over January, February, and March (colors) and surface wind stress (arrows) onto the first LFC of OHT for (a)–(f) CCSM4, (g)–(i) GFDL-ESM2M, and (j)–(l) HadGEM3. Lead times indicate anomalies that lead the LFC, i.e., prior to the maximum OHT. Because the LFCs are unitless, the regressions simply have units of Pa (per standard deviation).

(Figs. 14a–e). The anomalous AMOC then carries anomalously warm water northward into the subpolar gyre starting at lead 2 years. Concurrently, the subpolar gyre strengthens (Figs. 8a–e). The strengthened gyre circulation then carries this water into the Labrador Sea, where it eliminates the positive density anomalies and hence the deep convection (Figs. 13d–f). Meanwhile, a persistent cold, positive density anomaly forms in the Gulf Stream Extension region (Figs. 13d–f and 8d–f), suggesting a southward shift of the North Atlantic Current and Gulf Stream. Also, the gyre anomalies become concentrated around the boundary between the subpolar and subtropical gyres (Fig. 8f).

Owing to the increase in Labrador Sea surface density fluxes and WMT, AMOC strengthens at lead times in the high

latitudes, beginning around nine years before the maximum OHT (Figs. 14a–e). Given that the gyre circulation projects onto AMOC in density space, part of this signal is likely a result of the concurrent subpolar gyre strengthening (Figs. 8a–c). The AMOC anomaly extends throughout the North Atlantic, and is centered around 56°N and $\sigma_2 = 36.82$, where it reaches a maximum of 2.1 Sv (Fig. 14e). This is farther north and at a higher density than the maximum climatological AMOC. While the peak WMT anomaly is at a higher density class than the maximum AMOC anomaly, it still coincides with the large, broad AMOC anomaly. Leading up to the time of maximum OHT, this anomaly intensifies and spreads southward and to lower densities. AMOC reaches its maximum strength when
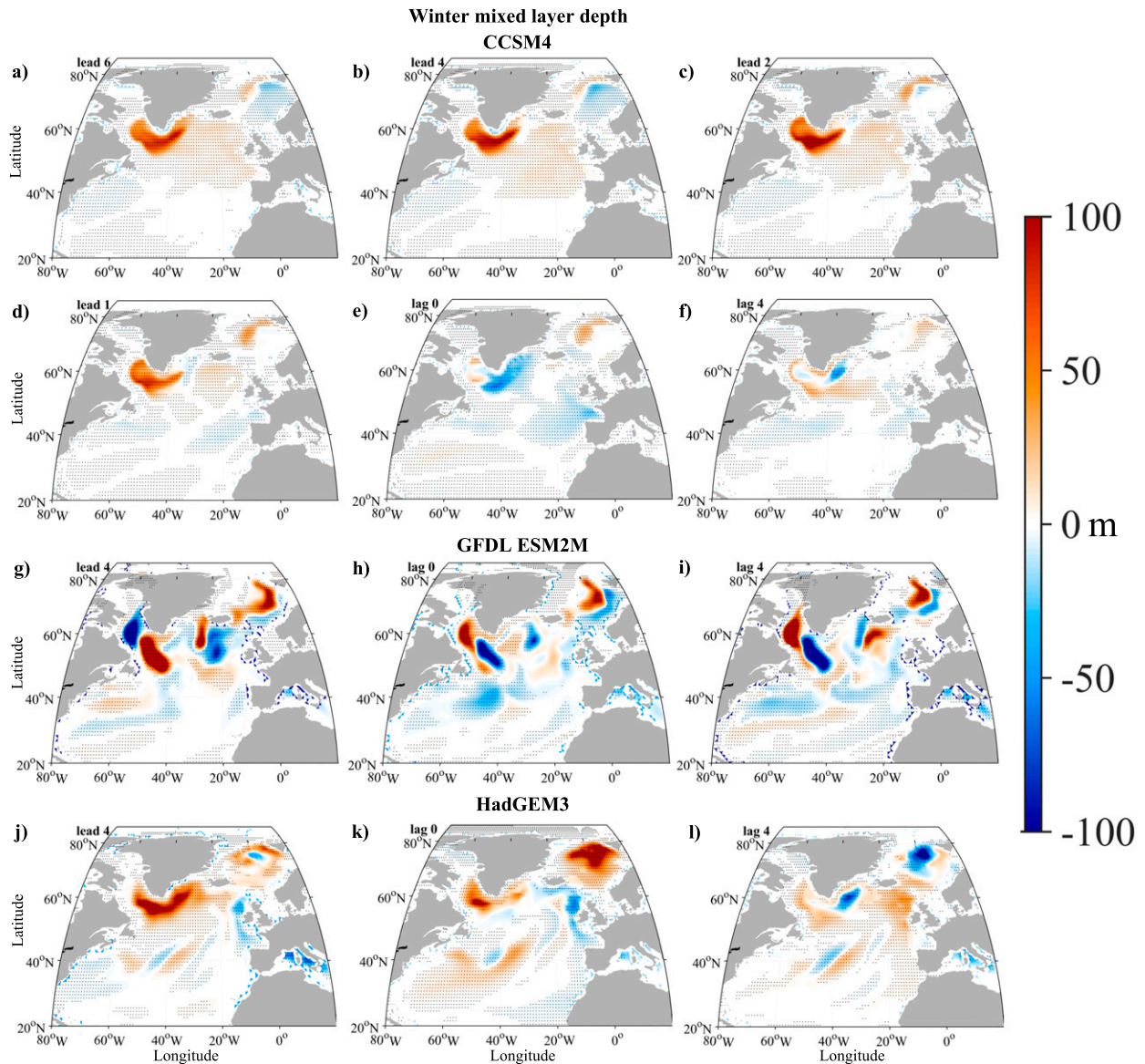
Winter mixed layer depth
CCSM4

FIG. 10. Lead–lag regressions of mixed layer depth averaged over January, February, and March onto the first LFC of OHT for (a)–(f) CCSM4, (g)–(i) GFDL-ESM2M, and (j)–(l) HadGEM3. Lead times indicate anomalies that lead the LFC, i.e., prior to the maximum OHT. Stippling indicates points where the regressions are statistically significant at the 95% level. Because the LFCs are unitless, the regressions simply have units of m (per standard deviation).

the OHT is at its maximum (i.e., at lag 0). At lag times, AMOC declines as a result of the reduced WMT in the Labrador Sea (Figs. 14e,f).

c. Comparison to mechanisms of low-frequency OHT variability in GFDL-ESM2M

Applying the same analysis to ESM2M, we find largely similar mechanisms of low-frequency OHT variability. As in CCSM4, OHT strengthens leading up to the time of maximum OHT (Fig. 7b). At lag times, OHT steadily decreases, as expected, eventually becoming negative at lag 6, indicating periodicity in this model's OHT variability (Fig. 7e). This has

been reported in previous studies (Dunne et al. 2012) and is evident as a peak in the OHT and AMOC power spectra at 15 years (not shown). This periodicity is not found in either of the other two GCMs examined here.

The SLP pattern at lead times is similar to what is found in CCSM4, with a high pressure system over the Labrador region of Canada driving anomalous northwesterly winds over the Labrador Sea (Fig. 9g), although the intense high pressure system found in CCSM4 at lag 0 is not found in ESM2M. Similar to CCSM4, SLP anomalies are weak at lag times (Fig. 9i), although ESM2M does show negative SLP anomalies throughout the North Atlantic.
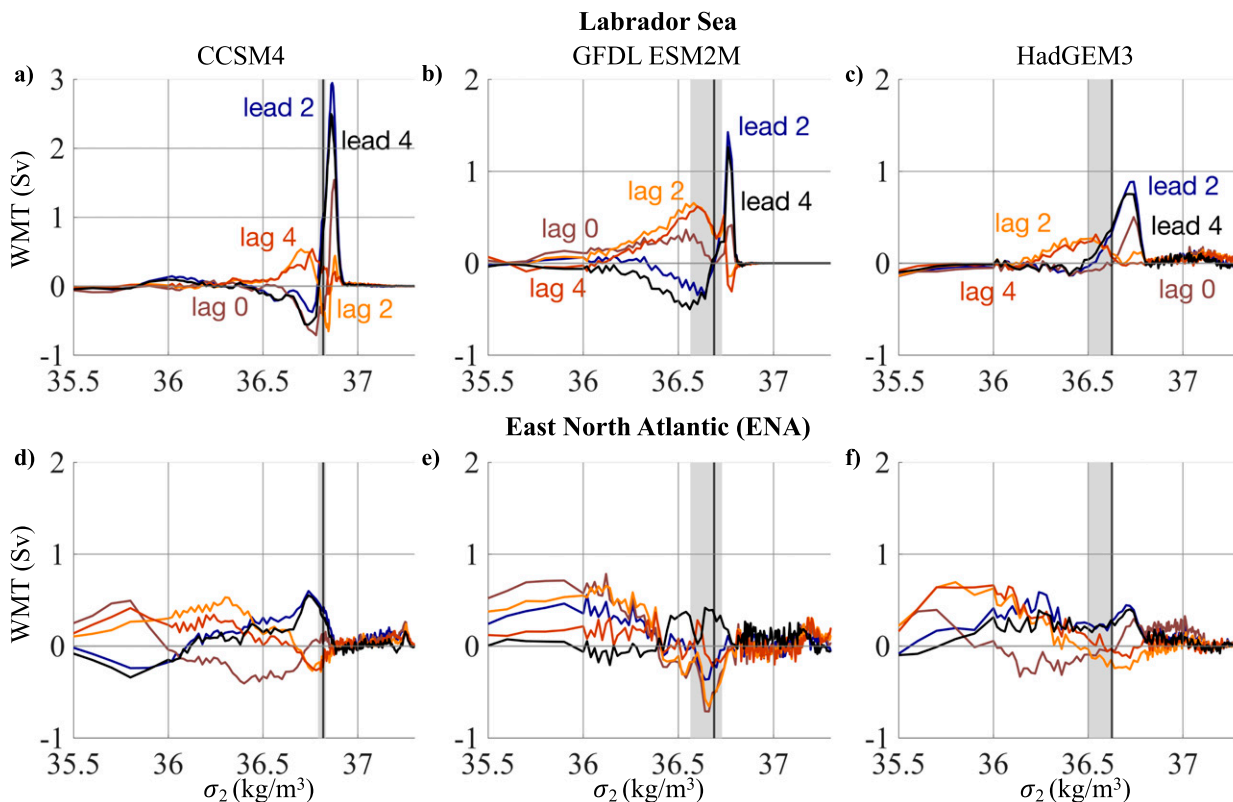
FIG. 11. Lead–lag regressions of water mass transformation (WMT) onto the first LFC of OHT for (left) CCSM4, (center) GFDL-ESM2M, and (right) HadGEM3. (a)–(c) WMT summed over the Labrador Sea region. (d)–(f) WMT summed over the eastern North Atlantic (ENA) section. The black vertical lines indicate the density where the AMOCσ regression at lag zero reaches its maximum in each model. The gray shaded areas represent the density range where the AMOCσ regression at lag zero is within 20% of its maximum value. The left and right boxes in Figs. 1a–c) represent what we consider to be the Labrador Sea and eastern North Atlantic (ENA) in this calculation. Lead times indicate anomalies that lead the LFC i.e., prior to the maximum OHT. Because the LFCs are unitless, the regressions simply have units of Sv (per standard deviation).

The anomalous northwesterly winds cause mixed layers in the southern Labrador Sea to deepen, although they shoal in the northern portion of the sea (Figs. 10g–i). This dipole pattern abruptly flips at lead 1 year, and then the new dipole pattern remains in place until lag 6. A dipole pattern also appears in the Iceland Basin at lead times, with deeper mixed layers to the west and shallower mixed layers to the east. This pattern flips at lead 1 and remains until lag 6.

Even though climatological WMT in GFDL-ESM2M is focused in the Irminger and Iceland Basins, the lagged regressions of WMT onto the first LFC look surprisingly similar to CCSM4, with a much more pronounced peak in the Labrador Sea at lead times than in the ENA box. The WMT anomaly in the Labrador Sea at lead 2 years is centered at $\sigma_2 = 36.76$ with a maximum value of 1.6 Sv. The WMT in the ENA starts out with a positive anomaly at lead 4 years, centered around $\sigma_2 = 36.68$ with a maximum value of 0.3 Sv, before it becomes negative at lead 2 years (Figs. 11b,e). The leading ENA WMT anomalies extend to much lower densities than the Labrador Sea WMT anomalies, which have a very narrow peak located at densities substantially higher than the peak in the AMOC anomaly at the time of maximum OHT (Figs. 11b,e). Both the

Labrador Sea and ENA WMT variability show substantial periodicity, as found with the other variables in this model. The WMT variability is dominated by heat flux changes, with freshwater flux changes playing a minor role (Figs. 12b,e).

The anomalous WMT and surface density fluxes over the Labrador Sea drive near-surface cooling and densification in the region at lead times (Fig. 13g), although they are less pronounced than in CCSM4. The concurrent increase in WMT and surface density fluxes cause AMOC to strengthen. Similar to CCSM4, the intensified AMOC increases the OHT, which then reduces the density anomalies and high-latitude deep convection (Figs. 13h,i). Meanwhile, density anomalies propagate southward along the western boundary (Figs. 13h,i), a process not seen in either of the other models.

Similar to CCSM4, AMOC begins to strengthen about six years prior to the maximum OHT. However, unlike in CCSM4, as the AMOC anomaly intensifies, it begins to propagate southward, similar to what is found for the density anomalies (Figs. 14g,h). At lag times, the AMOC anomaly rapidly dissipates and continues to propagate southward, after which it is replaced by a smaller negative AMOC anomaly at high latitudes (Fig. 14i), which we do not find in CCSM4. The AMOC

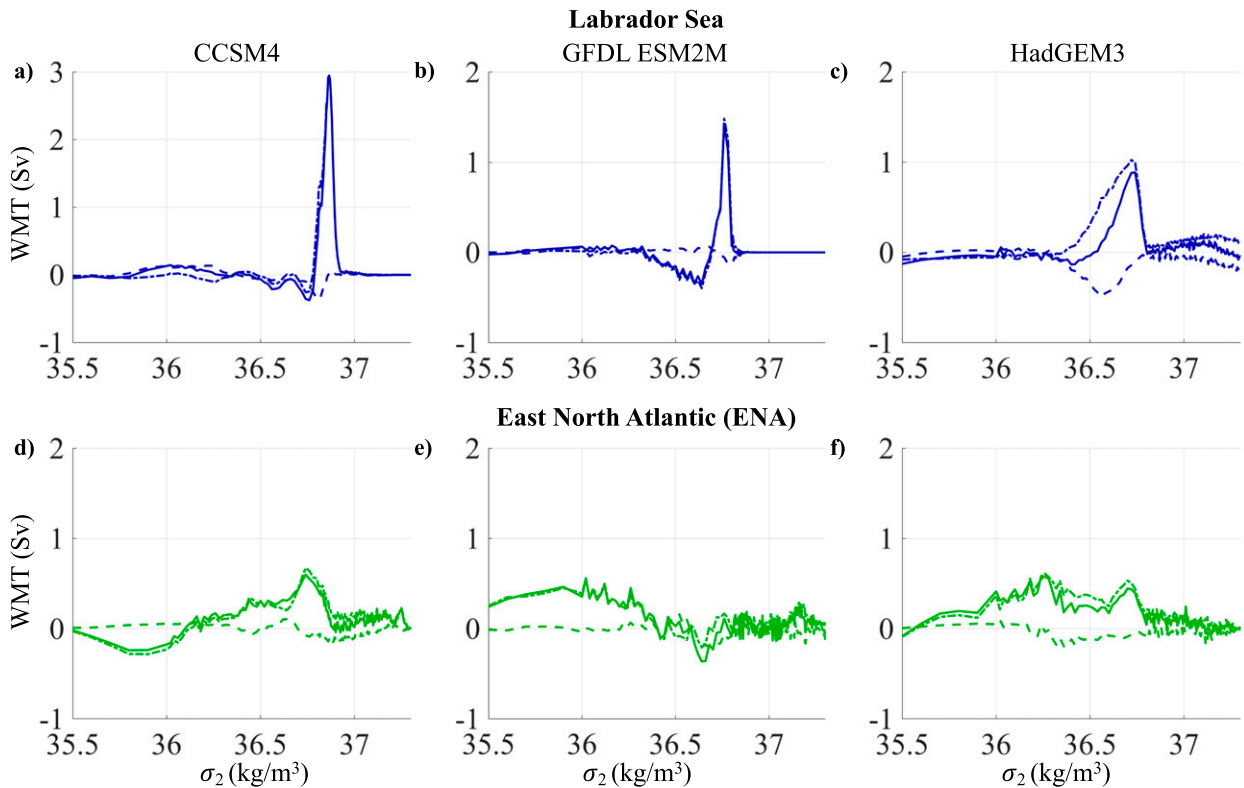**Labrador Sea**

East North Atlantic (ENA)

FIG. 12. 2-yr lead time regressions of thermal (dot-dashed lines), freshwater (dashed lines), and total (solid lines) WMT components onto the first LFC of OHT for (left) CCSM4, (center) GFDL-ESM2M, and (right) HadGEM3. (a)–(c) WMT summed over the Labrador Sea region. (d)–(f) WMT summed over the eastern North Atlantic (ENA). The left and right boxes in Figs. 1a–c represent what we consider to be the Labrador Sea and ENA in this calculation.

anomaly at the time of maximum OHT is centered around $\sigma_2 = 36.69$ and $\theta = 44.5°N$, with a maximum value of 2 Sv. This is south of and at a higher density class than the maximum climatological AMOC in this model.

Similar to CCSM4, while AMOC strengthens at lead times, both the subpolar and subtropical gyres strengthen and the subpolar gyre cools (Fig. 8g). Starting about one year before the maximum OHT, the barotropic streamfunction anomalies begin to congregate around the gyre boundary (not shown). These anomalies continue to propagate along the western boundary.

d. Comparison to mechanisms of low-frequency OHT variability in HadGEM3

For HadGEM3, OHT gradually strengthens leading up to the time of maximum OHT, maintaining a similar pattern with a very broad peak in the midlatitudes (Fig. 7c). At lag times, the OHT gradually weakens. This process is more gradual than it is in the other models (Fig. 7f).

The SLP pattern at lead times is similar to what is found in the other models, with a pronounced high pressure system over Labrador only occurring between lead 5 and lead 3 (Fig. 9j). At lead 1, this NAO-like pattern disappears and at lag zero there is a high pressure system over the eastern subpolar gyre and the Iceland Basin, similar to what is found in CCSM4, albeit much

weaker. Immediately after lag zero, the SLP anomalies become small (Fig. 9l), similar to what is found in the other two models.

Although the climatological WMT in HadGEM3 primarily occurs in the ENA (Fig. 3e), the WMT regressions at lead times show that much of the WMT variability at higher densities occurs in the Labrador Sea. There is a pronounced increase in WMT in the Labrador Sea at lead times, with a peak at lead 2 years, as in the other models. The anomaly at lead 2 years is centered at $\sigma_2 = 36.74$ with a maximum value of 0.9 Sv (Fig. 11c). There is also a peak in the ENA WMT at lead 2 centered around the same density, with a maximum magnitude equal to half of what is found in the Labrador Sea (i.e., 0.44 Sv; Fig. 11f). This peak is much broader than the peak in the Labrador Sea WMT, extending even to densities below $\sigma = 36$. As for the CCSM4 and ESM2M results above, the assessment of which region plays a dominant role in driving AMOC variability depends on which density ranges are considered to be important. The larger peak in WMT in the Labrador Sea, occurring at densities slightly higher than the peak density of AMOC variability (Fig. 11c), suggests that the Labrador Sea may play a larger role. However, this feature is not as pronounced as it is in CCSM4 and ESM2M, suggesting that the ENA may play a relatively large role in HadGEM3 compared to those other models. The WMT variability in this model is dominated by heat flux changes, although freshwater fluxes do contribute more than
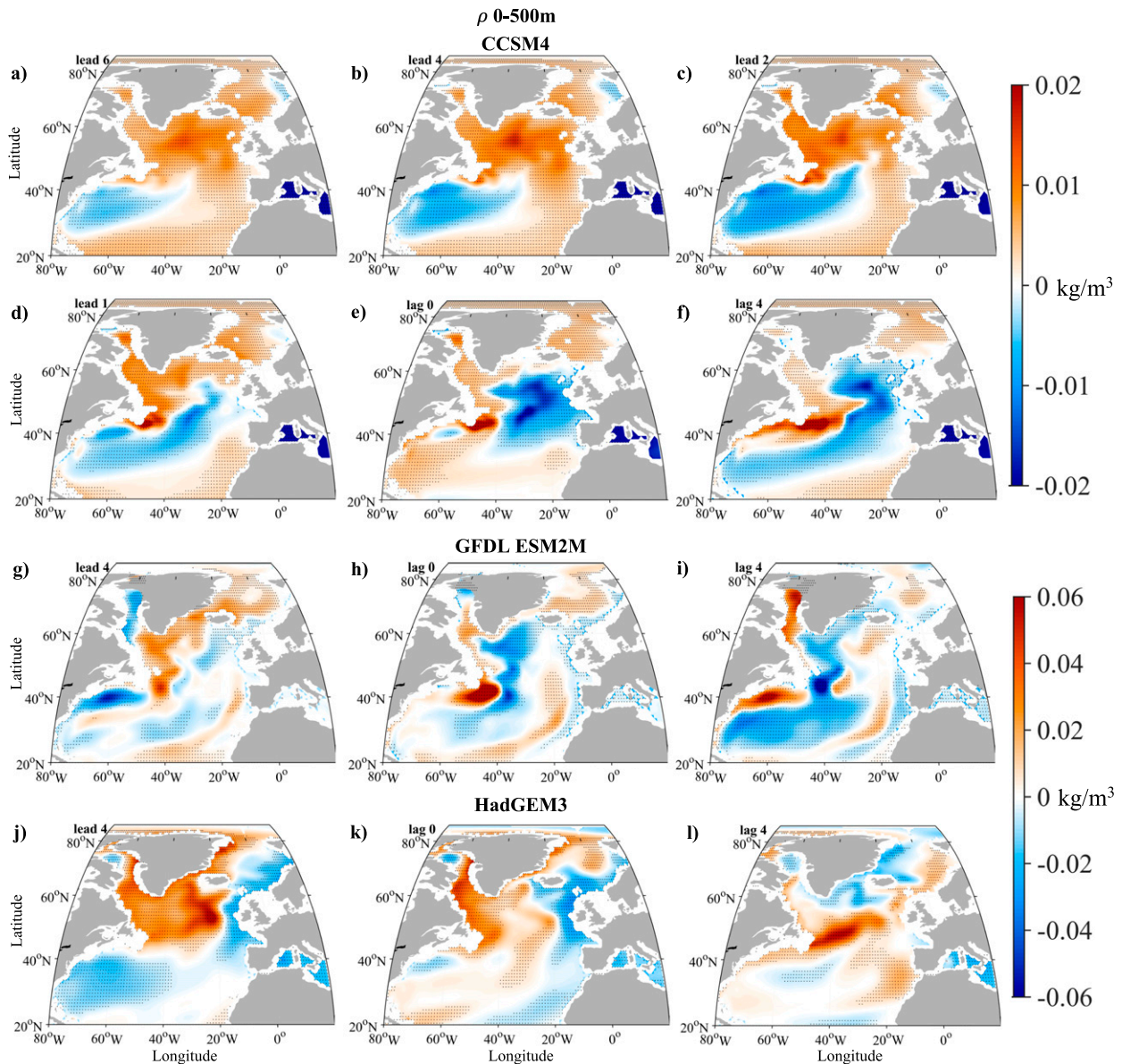
ρ **0–500m**
CCSM4

FIG. 13. Lead–lag regressions of water density averaged over 0–500 m onto the first LFC of OHT for (a)–(f) CCSM4, (g)–(i) GFDL-ESM2M, and (j)–(l) HadGEM3. Lead times indicate anomalies that lead the LFC, i.e., prior to the maximum OHT. Stippling indicates points where the regressions are statistically significant at the 95% level. Because the LFCs are unitless, the regressions simply have units of kg m^{-3} (per standard deviation).

in the other models (Figs. 12c,f), providing a small negative contribution to the WMT at lead times.

As seen in the other two GCMs, there is pronounced densification in both the Labrador Sea and the Irminger and Iceland Basins at lead times (Fig. 13j), peaking at lead 2 years. This coincides with increased WMT and surface density fluxes in these regions, strengthening AMOC, which then acts to weaken the high-latitude deep convection by carrying anomalously warm water northward. This warm water enters the subpolar gyre from the Iceland and Irminger Basins at the northeastern edge shortly after lag 0 (Fig. 13k), and is then

propagated westward, reaching the Labrador Sea at lag 4 years (Fig. 13l). This warm water does not have as pronounced of a density anomaly as seen in CCSM4. Similar to CCSM4, there is a persistent positive density anomaly in the Gulf Stream Extension region, and in contrast to ESM2M there is no southward propagation of upper ocean density anomalies.

Similar to CCSM4 and GFDL-ESM2M, at lead times there is a substantial deepening of the mixed layers in the Labrador Sea, peaking at lead 2 years before rapidly shoaling afterward (Figs. 10j,k). However, unlike in the other two models, mixed layers in the GIN Seas deepen at lead times as well, reaching
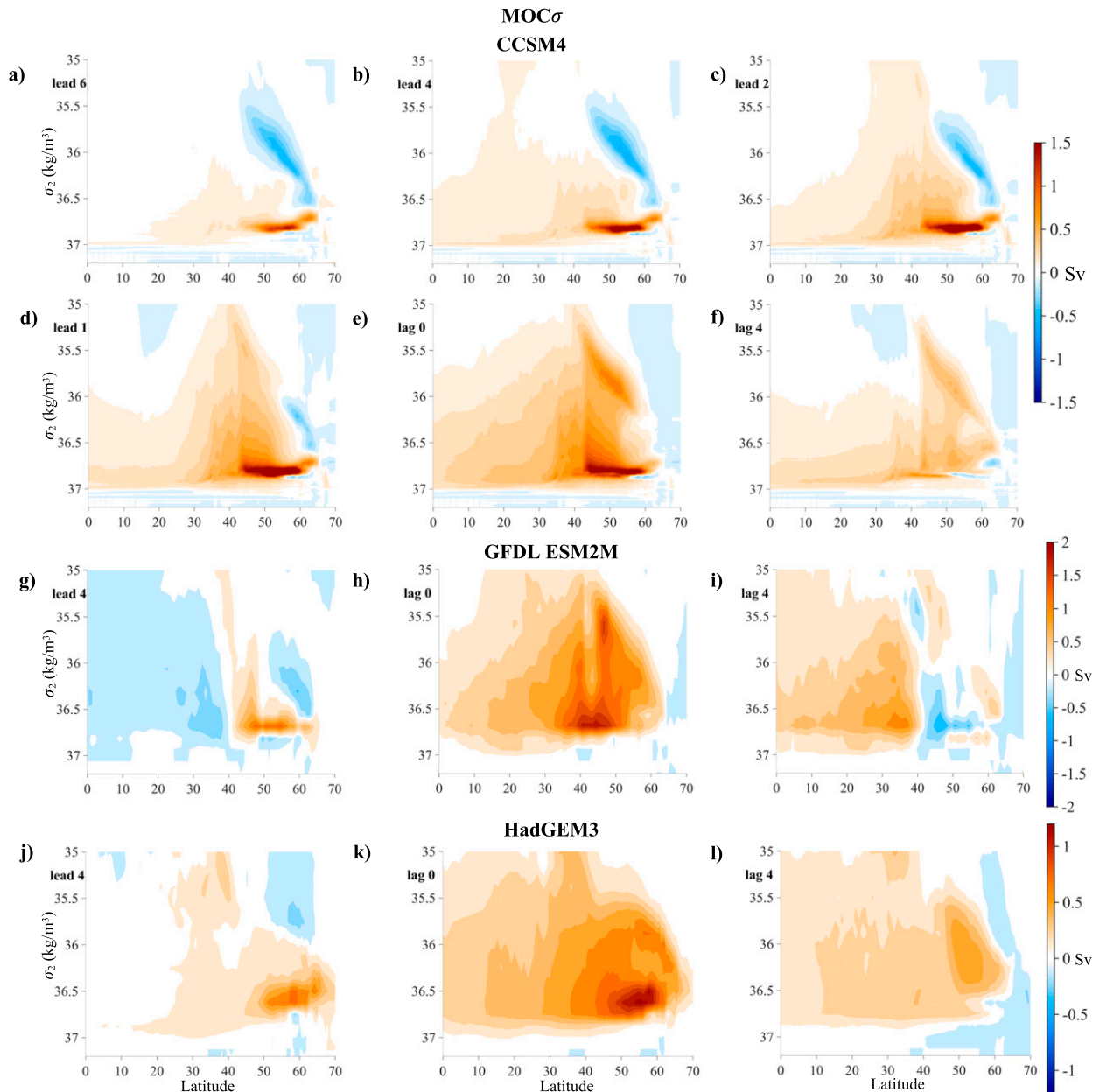
MOCσ
CCSM4

FIG. 14. Lead–lag regressions of the overturning streamfunction onto the first LFC of OHT for (a)–(f) CCSM4, (g)–(i) GFDL-ESM2M, and (j)–(l) HadGEM3. Lead times indicate anomalies that lead the LFC, i.e., prior to the maximum OHT. Because the LFCs are unitless, the regressions simply have units of Sv (per standard deviation).

their deepest at lag zero (Figs. 10j,k). After the time of maximum OHT, these mixed layers shoal as well (Fig. 10l).

As in CCSM4, AMOC strengthens at lead times, reaching a maximum at lag zero, coinciding with the time of maximum OHT (Figs. 14j,k). Afterward, AMOC steadily weakens as a result of the reduced WMT (Fig. 14l). The AMOC anomaly at the time of maximum OHT is centered around $\sigma_2 = 36.63$ and $\theta = 55.6°N$, with a maximum value of 1.3 Sv. This is north of and at a higher density class than the maximum climatological AMOC in this model.

At lead times, while AMOC strengthens, the subpolar gyre also strengthens, and at lag times the positive anomalies become more concentrated at the boundary between the subpolar and subtropical gyres (Figs. 8j–l), as seen in the other models.

5. Discussion and conclusions

Our results suggest a mechanism for low-frequency North Atlantic OHT variability that is consistent across the three

distinct GCMs used here: persistent SLP anomalies in the 4–9 years prior to the time of maximum OHT, which are associated with anomalous northwesterly winds off eastern North America that cool and densify the Labrador Sea waters through air–sea heat fluxes, coinciding with an increase in WMT in that region. This increased WMT causes AMOC to strengthen, increasing the OHT as a result. The strengthened AMOC carries anomalous warm water northward into the subpolar gyre, which then carries it into the Labrador Sea, where it shuts down the anomalous deep convection and associated WMT and weakens AMOC and OHT.

Although this mechanism is similar across the models, in GFDL-ESM2M there is pronounced periodicity in the density, AMOC, OHT, and water mass transformation variability. AMOC anomalies also appear to propagate southward in that model, consistent with what was found in Zhang (2010).

Our results suggest that AMOC variability is closely linked to preceding density anomalies in the subpolar gyre and the Labrador Sea, consistent with mechanisms discussed in Tulloch and Marshall (2012) and Kwon and Frankignoul (2014). However, our findings are not in agreement with those of Dong and Sutton (2005), who found a salinity-dominated mechanism in HadCM3, where a strengthened North Atlantic Current causes an increase in deep convection in the GIN Seas.

A comparison of WMT with observations indicates that biases in surface heat and freshwater fluxes play a much larger role than sea surface temperatures and salinities in setting the discrepancies between model and observation-based WMT in the ENA, with sea surface temperature and salinity biases playing a larger role in the Labrador Sea. Of the three models used here, HadGEM3 has the most realistic surface heat fluxes, sea surface temperatures, and salinities, though HadGEM3 heat fluxes in both the Labrador Sea and ENA are still larger than observational (OAFlux) estimates, and there are still substantial temperature and salinity biases in both regions in this model. HadGEM3's freshwater fluxes are not any more realistic than what is found in the other models. Given that HadGEM3 is the most realistic of the models, particular weight is added to the results of our low-frequency OHT variability analysis of that model.

The lead–lag regression analysis of water mass transformation suggests that regardless of a model's primary location of climatological convection and WMT, the Labrador Sea plays a major role in driving low-frequency AMOC and OHT variability. In CCSM4, climatological convection and WMT is concentrated in the Labrador Sea, and the GIN Seas and Irminger and Iceland Basins play a relatively minor role in driving the AMOC and OHT variability, although this conclusion is dependent on which density range is important for AMOC. In GFDL-ESM2M, climatological WMT is primarily in the Irminger and Iceland Basins, but the Labrador Sea still plays a substantial role in driving the AMOC variability, albeit with WMT anomalies concentrated at higher densities than the AMOC anomalies at the time of maximum OHT. In HadGEM3, the climatological WMT is mainly in the ENA, yet the Labrador Sea still contributes twice as much as the ENA to the WMT anomalies at higher densities, with ENA WMT anomalies more evenly spread across densities near where

AMOC reaches its maximum at the time of maximum OHT. While not all of the anomalous surface-forced WMT in the Labrador Sea necessarily translates to anomalous overturning owing to compensation from mixing processes, the robust lead–lag relationship between low-frequency OHT variability and WMT in the Labrador Sea suggests a mechanistic link. By applying the low-frequency component analysis to AMOC in each model instead of OHT, we find that WMT in the Labrador Sea also exhibits a clear lead–lag relationship with low-frequency AMOC variability (not shown). This analysis does not tell us the sensitivity of AMOC and OHT to changes in WMT in the Labrador Sea and ENA. Instead, it tells us the proportion of WMT variability in the different deepwater formation regions that is linked to low-frequency OHT variability. The fact that in CCSM4, for example, WMT variability in the ENA has only a very weak imprint on OHT does not indicate how sensitive OHT is to changes in WMT in the ENA, because there is very little WMT variability in this region in the model.

In CCSM4 and ESM2M, which both have warm, salty biases in the Labrador Sea relative to observations, heat fluxes dominate the WMT variability, consistent with what was found by Menary et al. (2015b). Heat fluxes also dominate the WMT variability in HadGEM3, even though this model does not have the same biases in the Labrador Sea. Freshwater fluxes play a more substantial role in the WMT climatology in HadGEM3, although the heat fluxes still dominate the variability.

Recent observations from the Overturning in the Subpolar North Atlantic Program (OSNAP) suggest that the Labrador Sea plays a minor role in driving the climatological overturning in the North Atlantic compared to the GIN Seas (Lozier et al. 2019; Zou et al. 2020). Zou et al. (2020) found that this is a consequence of density compensation in the Labrador Sea, where warm, salty water that enters the Labrador Sea exits as cold freshwater in the same density class. They also propose that large salinity biases in the Labrador Sea are responsible for the discrepancy between models and observations, as these biases may lead to a temperature dominated density structure, which is in agreement with our results in CCSM4. The OSNAP dataset is only 21 months long, and hence it was not possible to discern the mechanisms controlling decadal and multidecadal variability. Menary et al. (2020) show that high-latitude AMOC computed in both medium- and low-resolution HadGEM3 agrees well with AMOC computed from OSNAP data. Yet, the Labrador Sea features more predominantly in the low-frequency AMOC and OHT variability in HadGEM3 than would be expected based on its WMT climatology. This suggests that the Labrador Sea may play an important role in the low-frequency WMT, AMOC, and OHT variability in nature despite its limited role in setting the WMT and AMOC climatologies.

There are several caveats to our analysis. In this paper, when we analyze the link between WMT and AMOC, we choose to focus on WMT in the density range where AMOC is near its maximum. However, because we neglect mixing, we could be missing WMT contributions at other density classes which could cause the ENA to be more important. For example, there could be strong mixing in the ENA at lower density classes,

which would drive densification of lower-density water masses and also contribute to AMOC. There could also be concurrent mixing in the Labrador Sea that cancels out the surface-forced WMT there. Both CCSM4 and ESM2M have substantial temperature and salinity biases in the Labrador Sea (Menary et al. 2015b), which could distort the representation of deep convection and overturning in these models. The low-resolution models used here also likely overestimate Labrador Sea convection because they do not resolve eddies, which play a significant role in Labrador Sea stratification (Straneo 2006a; Brandt et al. 2007; Garcia-Quintana et al. 2019). Another issue is that Nordic seas overflow processes, which play an important role in AMOC and occur at relatively small spatial scales (Treguier et al. 2005; Langehaug et al. 2012a), are too weak in many low-resolution ocean models (Bailey et al. 2005). However, CCSM4 includes parameterized overflows (Danabasoglu et al. 2012a), yet still shows similar behavior to what is found in the other two models, which only use model resolved processes. Based on this, it would be valuable to perform a similar analysis in a high-resolution coupled model.

Here, we have found that the Labrador Sea plays a major role in low-frequency variability in water mass transformation, meridional overturning, and Atlantic OHT in three models with distinct primary climatological deep-water-formation regions. The results suggest that the Labrador Sea may play a larger role in AMOC and OHT variability than what would be expected based on its contribution to climatological WMT. The consensus between the three distinct models studied here, including a model which reproduces observed overturning in the eastern North Atlantic from the OSNAP program, suggests that the mechanisms that control decadal variability of the subpolar North Atlantic in these models may be representative of what is found in nature.

Data availability statement. The CMIP5 data for this study are accessible at the Earth System Grid Federation (ESGF) Portal (https://esgf-node.llnl.gov/search/cmip5/). The CMIP6 data for this study are accessible at the ESGF Portal (https://esgf-node.llnl.gov/search/cmip6/). EN4.2.1 sea surface temperature and salinity data (downloaded on 2 March 2020) are available at https://www.metoffice.gov.uk/hadobs/en4/index.html. OISST monthly sea surface temperature data are available at https://psl.noaa.gov/data/gridded/data.noaa.oisst.v2.html. OAFlux data are available at http://oaflux.whoi.edu/index.html. ERA5 data are available at https://climate.copernicus.eu/climate-reanalysis.

De Boyer climatological mixed layer depth is available at http://www.ifremer.fr/cerweb/deboyer/mld/home.php.

REFERENCES

Allen, M. R., and L. A. Smith, 1997: Optimal filtering in singular spectrum analysis. *Phys. Lett.*, **234A**, 419–428, https://doi.org/10.1016/S0375-9601(97)00559-8.

Ambaum, M. H. P., and B. J. Hoskins, 2002: The NAO troposphere–stratosphere connection. *J. Climate*, **15**, 1969–1978, https://doi.org/10.1175/1520-0442(2002)015<1969:TNTSC>2.0.CO;2.

Årthun, M., R. C. J. Wills, H. L. Johnson, L. Chafik, and H. R. Langehaug, 2021: Mechanisms of decadal North Atlantic climate variability and implications for the recent cold anomaly. *J. Climate*, **34**, 3421–3439, https://doi.org/10.1175/JCLI-D-20-0464.1.

Bailey, D. A., P. B. Rhines, and S. Häkkinen, 2005: Formation and pathways of North Atlantic deep water in a coupled ice–ocean model of the Arctic–North Atlantic Oceans. *Climate Dyn.*, **25**, 497–516, https://doi.org/10.1007/s00382-005-0050-3.

Bjerknes, J., 1964: Atlantic air–sea interaction. *Advances in Geophysics*, Vol. 10, Academic Press, 1–82, https://doi.org/10.1016/S0065-2687(08)60005-9.

Brambilla, E., and L. D. Talley, 2008: Subpolar mode water in the northeastern Atlantic: 1. Averaged properties and mean circulation. *J. Geophys. Res.*, **113**, C04025, https://doi.org/10.1029/2006JC004062.

Brandt, P., A. Funk, L. Czeschel, C. Eden, and C. W. Böning, 2007: Ventilation and transformation of Labrador Sea water and its rapid export in the deep Labrador Current. *J. Phys. Oceanogr.*, **37**, 946–961, https://doi.org/10.1175/JPO3044.1.

Brodeau, L., and T. Koenigk, 2016: Extinction of the northern oceanic deep convection in an ensemble of climate model simulations of the 20th and 21st centuries. *Climate Dyn.*, **46**, 2863–2882, https://doi.org/10.1007/s00382-015-2736-5.

Cane, M. A., A. C. Clement, L. N. Murphy, and K. Bellomo, 2017: Low-pass filtering, heat flux, and Atlantic multidecadal variability. *J. Climate*, **30**, 7529–7553, https://doi.org/10.1175/JCLI-D-16-0810.1.

Chafik, L., and T. Rossby, 2019: Volume, heat, and freshwater divergences in the subpolar North Atlantic suggest the Nordic seas as key to the state of the meridional overturning circulation. *Geophys. Res. Lett.*, **46**, 4799–4808, https://doi.org/10.1029/2019GL082110.

Covey, C., and S. L. Thompson, 1989: Testing the effects of ocean heat transport on climate. *Global Planet. Change*, **1**, 331–341, https://doi.org/10.1016/0921-8181(89)90009-X.

Danabasoglu, G., S. C. Bates, B. P. Briegleb, S. R. Jayne, M. Jochum, W. G. Large, S. Peacock, and S. G. Yeager, 2012a: The CCSM4 ocean component. *J. Climate*, **25**, 1361–1389, https://doi.org/10.1175/JCLI-D-11-00091.1.

——, S. G. Yeager, Y.-O. Kwon, J. J. Tribbia, A. S. Phillips, and J. W. Hurrell, 2012b: Variability of the Atlantic meridional overturning circulation in CCSM4. *J. Climate*, **25**, 5153–5172, https://doi.org/10.1175/JCLI-D-11-00463.1.

Day, J. J., J. C. Hargreaves, J. D. Annan, and A. Abe-Ouchi, 2012: Sources of multi-decadal variability in Arctic sea ice extent. *Environ. Res. Lett.*, **7**, 034011, https://doi.org/10.1088/1748-9326/7/3/034011.

de Boyer Montégut, C., G. Madec, A. S. Fischer, A. Lazar, and D. Iudicone, 2004: Mixed layer depth over the global ocean: An examination of profile data and a profile-based climatology. *J. Geophys. Res.*, **109**, C12003, https://doi.org/10.1029/2004JC002378.

——, J. Mignot, A. Lazar, and S. Cravatte, 2007: Control of salinity on the mixed layer depth in the world ocean: 1. General description. *J. Geophys. Res.*, **112**, C06011, https://doi.org/10.1029/2006JC003953.

Delworth, T. L., and F. Zeng, 2016: The impact of the North Atlantic Oscillation on climate through its influence on the Atlantic meridional overturning circulation. *J. Climate*, **29**, 941–962, https://doi.org/10.1175/JCLI-D-15-0396.1.

——, S. Manabe, and R. J. Stouffer, 1993: Interdecadal variations of the thermohaline circulation in a coupled ocean–atmosphere model. *J. Climate*, **6**, 1993–2011, https://doi.org/10.1175/1520-0442(1993)006<1993:IVOTTC>2.0.CO;2.

——, R. Zhang, and M. E. Mann, 2007: Decadal to centennial variability of the Atlantic from observations and models. *Ocean Circulation: Mechanisms and Impacts—Past and Future Changes of Meridional Overturning*, Geophys. Monogr., Vol. 173, Amer. Geophys. Union, 131–148.

——, F. Zeng, G. A. Vecchi, X. Yang, L. Zhang, and R. Zhang, 2016: The North Atlantic Oscillation as a driver of rapid climate change in the Northern Hemisphere. *Nat. Geosci.*, **9**, 509–512, https://doi.org/10.1038/ngeo2738.

Deser, C., M. A. Alexander, S.-P. Xie, and A. S. Phillips, 2010: Sea surface temperature variability: Patterns and mechanisms. *Annu. Rev. Mar. Sci.*, **2**, 115–143, https://doi.org/10.1146/annurev-marine-120408-151453.

Docquier, D., and Coauthors, 2019: Impact of model resolution on Arctic sea ice and North Atlantic Ocean heat transport. *Climate Dyn.*, **53**, 4989–5017, https://doi.org/10.1007/s00382-019-04840-y.

Dong, B., and R. T. Sutton, 2001: The dominant mechanisms of variability in Atlantic Ocean heat transport in a coupled ocean–atmosphere GCM. *Geophys. Res. Lett.*, **28**, 2445–2448, https://doi.org/10.1029/2000GL012531.

——, and ——, 2002: Variability in North Atlantic heat content and heat transport in a coupled ocean–atmosphere GCM. *Climate Dyn.*, **19**, 485–497, https://doi.org/10.1007/s00382-002-0239-7.

——, and ——, 2003: Variability of Atlantic Ocean heat transport and its effects on the atmosphere. *Ann. Geophys.*, **46**, 87–97, https://doi.org/10.4401/ag-3391.

——, and ——, 2005: Mechanism of interdecadal thermohaline circulation variability in a coupled ocean–atmosphere GCM. *J. Climate*, **18**, 1117–1135, https://doi.org/10.1175/JCLI3328.1.

Drijfhout, S. S., and W. Hazeleger, 2006: Changes in MOC and gyre-induced Atlantic Ocean heat transport. *Geophys. Res. Lett.*, **33**, L07707, https://doi.org/10.1029/2006GL025807.

Dunne, J. P., and Coauthors, 2012: GFDL's ESM2 global coupled climate–carbon Earth system models. Part I: Physical formulation and baseline simulation characteristics. *J. Climate*, **25**, 6646–6665, https://doi.org/10.1175/JCLI-D-11-00560.1.

——, and Coauthors, 2013: GFDL's ESM2 global coupled climate–carbon Earth system models. Part II: Carbon system formulation and baseline simulation characteristics. *J. Climate*, **26**, 2247–2267, https://doi.org/10.1175/JCLI-D-12-00150.1.

Ebisuzaki, W., 1997: A method to estimate the statistical significance of a correlation when the data are serially correlated. *J. Climate*, **10**, 2147–2153, https://doi.org/10.1175/1520-0442(1997)010<2147:AMTETS>2.0.CO;2.

Eden, C., and T. Jung, 2001: North Atlantic interdecadal variability: Oceanic response to the North Atlantic Oscillation (1865–1997). *J. Climate*, **14**, 676–691, https://doi.org/10.1175/1520-0442(2001)014<0676:NAIVOR>2.0.CO;2.

Ganachaud, A., and C. Wunsch, 2000: Improved estimates of global ocean circulation, heat transport and mixing from hydrographic data. *Nature*, **408**, 453–457, https://doi.org/10.1038/35044048.

——, and ——, 2003: Large-scale ocean heat and freshwater transports during the World Ocean Circulation Experiment. *J. Climate*, **16**, 696–705, https://doi.org/10.1175/1520-0442(2003)016<0696:LSOHAF>2.0.CO;2.

Garcia-Quintana, Y., P. Courtois, X. Hu, C. Pennelly, D. Kieke, and P. G. Myers, 2019: Sensitivity of Labrador Sea water formation to changes in model resolution, atmospheric forcing, and freshwater input. *J. Geophys. Res. Oceans*, **124**, 2126–2152, https://doi.org/10.1029/2018JC014459.

Gent, P. R., and Coauthors, 2011: The Community Climate System Model version 4. *J. Climate*, **24**, 4973–4991, https://doi.org/10.1175/2011JCLI4083.1.

Good, S. A., M. J. Martin, and N. A. Rayner, 2013: EN4: Quality controlled ocean temperature and salinity profiles and monthly objective analyses with uncertainty estimates. *J. Geophys. Res. Oceans*, **118**, 6704–6716, https://doi.org/10.1002/2013JC009067.

Grist, J. P., R. Marsh, and S. A. Josey, 2009: On the relationship between the North Atlantic meridional overturning circulation and the surface-forced overturning streamfunction. *J. Climate*, **22**, 4989–5002, https://doi.org/10.1175/2009JCLI2574.1.

Hersbach, H., and D. Dee, 2016: ERA5 reanalysis is in production. *ECMWF Newsletter*, No. 147, ECMWF, Reading, United Kingdom, 7, http://www.ecmwf.int/sites/default/files/elibrary/2016/16299-newsletter-no147-spring-2016.pdf.

Heuzé, C., 2017: North Atlantic deep water formation and AMOC in CMIP5 models. *Ocean Sci.*, **13**, 609–622, https://doi.org/10.5194/os-13-609-2017.

Isachsen, P. E., C. Mauritzen, and H. Svendsen, 2007: Dense water formation in the Nordic seas diagnosed from sea surface buoyancy fluxes. *Deep-Sea Res. I*, **54**, 22–41, https://doi.org/10.1016/j.dsr.2006.09.008.

Jackson, L. C., and Coauthors, 2020: Impact of ocean resolution and mean state on the rate of AMOC weakening. *Climate Dyn.*, **55**, 1711–1732, https://doi.org/10.1007/s00382-020-05345-9.

Josey, S. A., J. P. Grist, and R. Marsh, 2009: Estimates of meridional overturning circulation variability in the North Atlantic from surface density flux fields. *J. Geophys. Res.*, **114**, C09022, https://doi.org/10.1029/2008JC005230.

Kim, W. M., S. Yeager, P. Chang, and G. Danabasoglu, 2018: Low-frequency North Atlantic climate variability in the Community Earth System Model large ensemble. *J. Climate*, **31**, 787–813, https://doi.org/10.1175/JCLI-D-17-0193.1.

——, ——, and G. Danabasoglu, 2020: Atlantic multidecadal variability and associated climate impacts initiated by ocean thermohaline dynamics. *J. Climate*, **33**, 1317–1334, https://doi.org/10.1175/JCLI-D-19-0530.1.

Knight, J. R., R. J. Allan, C. K. Folland, M. Vellinga, and M. E. Mann, 2005: A signature of persistent natural thermohaline circulation cycles in observed climate. *Geophys. Res. Lett.*, **32**, L20708, https://doi.org/10.1029/2005GL024233.

Koenigk, T., and Coauthors, 2020: Deep water formation in the North Atlantic Ocean in high resolution global coupled climate models. *Ocean Sci. Discuss.*, https://doi.org/10.5194/os-2020-41.

Kuhlbrodt, T., and Coauthors, 2018: The low-resolution version of HadGEM3 GC3.1: Development and evaluation for global climate. *J. Adv. Model. Earth Syst.*, **10**, 2865–2888, https://doi.org/10.1029/2018MS001370.

Kushnir, Y., 1994: Interdecadal variations in North Atlantic sea surface temperature and associated atmospheric conditions. *J. Climate*, **7**, 141–157, https://doi.org/10.1175/1520-0442(1994)007<0141:IVINAS>2.0.CO;2.

Kwon, Y.-O., and C. Frankignoul, 2014: Mechanisms of multidecadal Atlantic meridional overturning circulation variability diagnosed in depth versus density space. *J. Climate*, **27**, 9359–9376, https://doi.org/10.1175/JCLI-D-14-00228.1.

Langehaug, H. R., I. Medhaug, T. Eldevik, and O. H. Otterå, 2012a: Arctic/Atlantic exchanges via the subpolar gyre. *J. Climate*, **25**, 2421–2439, https://doi.org/10.1175/JCLI-D-11-00085.1.

——, P. B. Rhines, T. Eldevik, J. Mignot, and K. Lohmann, 2012b: Water mass transformation and the North Atlantic Current in three multicentury climate model simulations. *J. Geophys. Res.*, **117**, C11001, https://doi.org/10.1029/2012JC008021.

Large, W. G., J. C. McWilliams, and S. C. Doney, 1994: Oceanic vertical mixing: A review and a model with a nonlocal boundary layer parameterization. *Rev. Geophys.*, **32**, 363–403, https://doi.org/10.1029/94RG01872.

Levitus, S., 1983: Climatological atlas of the World Ocean. *Eos, Trans. Amer. Geophys. Union*, **64**, 962–963, https://doi.org/10.1029/EO064i049p00962-02.

Li, F., M. S. Lozier, G. Danabasoglu, N. P. Holliday, Y.-O. Kwon, A. Romanou, S. G. Yeager, and R. Zhang, 2019: Local and downstream relationships between Labrador Sea water volume and North Atlantic meridional overturning circulation variability. *J. Climate*, **32**, 3883–3898, https://doi.org/10.1175/JCLI-D-18-0735.1.

Lozier, M. S., and Coauthors, 2019: A sea change in our view of overturning in the subpolar North Atlantic. *Science*, **363**, 516–521, https://doi.org/10.1126/science.aau6592.

MacMartin, D. G., E. Tziperman, and L. Zanna, 2013: Frequency domain multimodel analysis of the response of Atlantic meridional overturning circulation to surface forcing. *J. Climate*, **26**, 8323–8340, https://doi.org/10.1175/JCLI-D-12-00717.1.

——, L. Zanna, and E. Tziperman, 2016: Suppression of Atlantic meridional overturning circulation variability at increased CO_2. *J. Climate*, **29**, 4155–4164, https://doi.org/10.1175/JCLI-D-15-0533.1.

Marsh, R., 2000: Recent variability of the North Atlantic thermohaline circulation inferred from surface heat and freshwater fluxes. *J. Climate*, **13**, 3239–3260, https://doi.org/10.1175/1520-0442(2000)013<3239:RVOTNA>2.0.CO;2.

McCartney, M. S., and L. D. Talley, 1982: The subpolar mode water of the North Atlantic Ocean. *J. Phys. Oceanogr.*, **12**, 1169–1188, https://doi.org/10.1175/1520-0485(1982)012<1169:TSMWOT>2.0.CO;2.

Mecking, J. V., N. S. Keenlyside, and R. J. Greatbatch, 2015: Multiple timescales of stochastically forced North Atlantic Ocean variability: A model study. *Ocean Dyn.*, **65**, 1367–1381, https://doi.org/10.1007/s10236-015-0868-0.

Menary, M. B., D. L. R. Hodson, J. I. Robson, R. T. Sutton, and R. A. Wood, 2015a: A mechanism of internal decadal Atlantic Ocean variability in a high-resolution coupled climate model. *J. Climate*, **28**, 7764–7785, https://doi.org/10.1175/JCLI-D-15-0106.1.

——, ——, ——, ——, and J. A. Hunt, 2015b: Exploring the impact of CMIP5 model biases on the simulation of North Atlantic decadal variability. *Geophys. Res. Lett.*, **42**, 5926–5934, https://doi.org/10.1002/2015GL064360.

——, and Coauthors, 2018: Preindustrial control simulations with HadGEM3-GC3.1 for CMIP6. *J. Adv. Model. Earth Syst.*, **10**, 3049–3075, https://doi.org/10.1029/2018MS001495.

——, L. C. Jackson, and M. S. Lozier, 2020: Reconciling the relationship between the AMOC and Labrador Sea in OSNAP observations and climate models. *Geophys. Res. Lett.*, **47**, e2020GL08979, https://doi.org/10.1029/2020GL089793.

Mignot, J., C. de Boyer Montégut, A. Lazar, and S. Cravatte, 2007: Control of salinity on the mixed layer depth in the world ocean: 2. Tropical areas. *J. Geophys. Res.*, **112**, C10010, https://doi.org/10.1029/2006JC003954.

Msadek, R., W. E. Johns, S. G. Yeager, G. Danabasoglu, T. L. Delworth, and A. Rosati, 2013: The Atlantic meridional heat transport at 26.5°N and its relationship with the MOC in the RAPID array and the GFDL and NCAR coupled models. *J. Climate*, **26**, 4335–4356, https://doi.org/10.1175/JCLI-D-12-00081.1.

Nurser, A. J. G., R. Marsh, and R. G. Williams, 1999: Diagnosing water mass formation from air–sea fluxes and surface mixing. *J. Phys. Oceanogr.*, **29**, 1468–1487, https://doi.org/10.1175/1520-0485(1999)029<1468:DWMFFA>2.0.CO;2.

Oldenburg, D., K. C. Armour, L. Thompson, and C. M. Bitz, 2018: Distinct mechanisms of ocean heat transport into the Arctic under internal variability and climate change. *Geophys. Res. Lett.*, **45**, 7692–7700, https://doi.org/10.1029/2018GL078719.

Peixoto, J. P., and A. H. Oort, 1993: *Physics of Climate*. American Institute of Physics, 520 pp.

Pérez-Brunius, P., T. Rossby, and D. R. Watts, 2004: Transformation of the warm waters of the North Atlantic from a geostrophic streamfunction perspective. *J. Phys. Oceanogr.*, **34**, 2238–2256, https://doi.org/10.1175/1520-0485(2004)034<2238:TOTWWO>2.0.CO;2.

Petit, T., M. S. Lozier, S. A. Josey, and S. A. Cunningham, 2020: Atlantic deep water formation occurs primarily in the Iceland basin and Irminger Sea by local buoyancy forcing. *Geophys. Res. Lett.*, **47**, e2020GL091028, https://doi.org/10.1029/2020GL091028.

Pickart, R. S., and M. A. Spall, 2007: Impact of Labrador Sea convection on the North Atlantic meridional overturning circulation. *J. Phys. Oceanogr.*, **37**, 2207–2227, https://doi.org/10.1175/JPO3178.1.

Reynolds, R. W., N. A. Rayner, T. M. Smith, D. C. Stokes, and W. Wang, 2002: An improved in situ and satellite SST analysis for climate. *J. Climate*, **15**, 1609–1625, https://doi.org/10.1175/1520-0442(2002)015<1609:AIISAS>2.0.CO;2.

Roberts, M. J., and Coauthors, 2019: Description of the resolution hierarchy of the global coupled HadGEM3-GC3.1 model as used in CMIP6 HighResMIP experiments. *Geosci. Model Dev.*, **12**, 4999–5028, https://doi.org/10.5194/gmd-12-4999-2019.

——, and Coauthors, 2020: Sensitivity of the Atlantic meridional overturning circulation to model resolution in CMIP6 HighResMIP simulations and implications for future changes. *J. Adv. Model. Earth Syst.*, **12**, e2019MS002014, https://doi.org/10.1029/2019MS002014.

Schlesinger, M. E., and N. Ramankutty, 1994: An oscillation in the global climate system of period 65–70 years. *Nature*, **367**, 723–726, https://doi.org/10.1038/367723a0.

Schneider, T., and S. Griffies, 1999: A conceptual framework for predictability studies. *J. Climate*, **12**, 3133–3155, https://doi.org/10.1175/1520-0442(1999)012<3133:ACFFPS>2.0.CO;2.

——, and I. M. Held, 2001: Discriminants of twentieth-century changes in Earth surface temperatures. *J. Climate*, **14**, 249–254, https://doi.org/10.1175/1520-0442(2001)014<0249:LDOTCC>2.0.CO;2.

Speer, K., and E. Tziperman, 1992: Rates of water mass formation in the North Atlantic Ocean. *J. Phys. Oceanogr.*, **22**, 93–104, https://doi.org/10.1175/1520-0485(1992)022<0093:ROWMFI>2.0.CO;2.

Straneo, F., 2006a: Heat and freshwater transport through the central Labrador Sea. *J. Phys. Oceanogr.*, **36**, 606–628, https://doi.org/10.1175/JPO2875.1.

——, 2006b: On the connection between dense water formation, overturning, and poleward heat transport in a convective basin. *J. Phys. Oceanogr.*, **36**, 1822–1840, https://doi.org/10.1175/JPO2932.1.

Tandon, A., and L. Zhao, 2004: Mixed layer transformation for the North Atlantic for 1990–2000. *J. Geophys. Res.*, **109**, C05018, https://doi.org/10.1029/2003JC002059.

Taylor, K. E., R. J. Stouffer, and G. A. Meehl, 2012: An overview of CMIP5 and the experiment design. *Bull. Amer. Meteor. Soc.*, **93**, 485–498, https://doi.org/10.1175/BAMS-D-11-00094.1.

Ting, M., Y. Kushnir, R. Seager, and C. Li, 2009: Forced and internal twentieth-century SST trends in the North Atlantic. *J. Climate*, **22**, 1469–1481, https://doi.org/10.1175/2008JCLI2561.1.

Treguier, A. M., S. Theetten, E. P. Chassignet, T. Penduff, R. Smith, L. Talley, J. O. Beismann, and C. Böning, 2005: The North Atlantic subpolar gyre in four high-resolution models. *J. Phys. Oceanogr.*, **35**, 757–774, https://doi.org/10.1175/JPO2720.1.

Tulloch, R., and J. Marshall, 2012: Exploring mechanisms of variability and predictability of Atlantic meridional overturning circulation in two coupled climate models. *J. Climate*, **25**, 4067–4080, https://doi.org/10.1175/JCLI-D-11-00460.1.

Tziperman, E., 1986: On the role of interior mixing and air–sea fluxes in determining the stratification and circulation of the oceans. *J. Phys. Oceanogr.*, **16**, 680–693, https://doi.org/10.1175/1520-0485(1986)016<0680:OTROIM>2.0.CO;2.

Venzke, S., M. R. Allen, R. T. Sutton, and D. P. Rowell, 1999: The atmospheric response over the North Atlantic to decadal changes in sea surface temperature. *J. Climate*, **12**, 2562–2584, https://doi.org/10.1175/1520-0442(1999)012<2562:TAROTN>2.0.CO;2.

Vörösmarty, C., B. Fekete, M. Meybeck, and R. Lammers, 2000: Geomorphometric attributes of the global system of rivers at 30-minute spatial resolution. *J. Hydrol.*, **237**, 17–39, https://doi.org/10.1016/S0022-1694(00)00282-1.

Walin, G., 1982: On the relation between sea-surface heat flow and thermal circulation in the ocean. *Tellus*, **34**, 187–195, https://doi.org/10.3402/tellusa.v34i2.10801.

Wills, R. C., and T. Schneider, 2015: Stationary eddies and the zonal asymmetry of net precipitation and ocean freshwater forcing. *J. Climate*, **28**, 5115–5133, https://doi.org/10.1175/JCLI-D-14-00573.1.

——, ——, J. M. Wallace, D. S. Battisti, and D. L. Hartmann, 2018: Disentangling global warming, multidecadal variability, and El Niño in Pacific temperatures. *Geophys. Res. Lett.*, **45**, 2487–2496, https://doi.org/10.1002/2017GL076327.

——, K. C. Armour, D. S. Battisti, and D. L. Hartmann, 2019a: Ocean–atmosphere dynamical coupling fundamental to the Atlantic multidecadal oscillation. *J. Climate*, **32**, 251–272, https://doi.org/10.1175/JCLI-D-18-0269.1.

——, D. S. Battisti, C. Proistosescu, L. Thompson, D. L. Hartmann, and K. C. Armour, 2019b: Ocean circulation signatures of North Pacific decadal variability. *Geophys. Res. Lett.*, **46**, 1690–1701, https://doi.org/10.1029/2018GL080716.

Xu, X., P. B. Rhines, and E. P. Chassignet, 2018: On mapping the diapycnal water mass transformation of the upper North Atlantic Ocean. *J. Phys. Oceanogr.*, **48**, 2233–2258, https://doi.org/10.1175/JPO-D-17-0223.1.

Yan, X., R. Zhang, and T. R. Knutson, 2018: Underestimated AMOC variability and implications for AMV and predictability in CMIP models. *Geophys. Res. Lett.*, **45**, 4319–4328, https://doi.org/10.1029/2018GL077378.

Yu, L., X. Jin, and R. A. Weller, 2008: Multidecade global flux datasets from the Objectively Analyzed Air–Sea Fluxes (OAFlux) project: Latent and sensible heat fluxes, ocean evaporation, and related surface meteorological variables. OAFlux Project Tech. Rep., OA-2008-01, 64 pp., http://oaflux.whoi.edu/pdfs/OAFlux_TechReport_3rd_release.pdf.

Zhang, L., and C. Wang, 2013: Multidecadal North Atlantic sea surface temperature and Atlantic meridional overturning circulation variability in CMIP5 historical simulations. *J. Geophys. Res. Oceans*, **118**, 5772–5791, https://doi.org/10.1002/jgrc.20390.

Zhang, R., 2010: Latitudinal dependence of Atlantic meridional overturning circulation (AMOC) variations. *Geophys. Res. Lett.*, **37**, L16703, https://doi.org/10.1029/2010GL044474.

——, 2015: Mechanisms for low-frequency variability of summer Arctic sea ice extent. *Proc. Natl. Acad. Sci. USA*, **112**, 4570–4575, https://doi.org/10.1073/pnas.1422296112.

Zou, S., M. S. Lozier, F. Li, R. Abernathey, and L. Jackson, 2020: Density-compensated overturning in the Labrador Sea. *Nat. Geosci.*, **13**, 121–126, https://doi.org/10.1038/s41561-019-0517-1.